JOURNAL OF PETROLOGY | VOLUME 00 | NUMBER 0 | PAGES 000–000 | 2007 | doi:10.1093/petrology/egm065
Journal of Petrology Advance Access published November 6, 2007

Stress-driven Melt Segregation and Strain Partitioning in Partially Molten Rocks: Effects of Stress and Strain

BENJAMIN K. HOLTZMAN* AND DAVID L. KOHLSTEDT

DEPARTMENT OF GEOLOGY & GEOPHYSICS, UNIVERSITY OF MINNESOTA, 310 PILLSBURY DRIVE SE, MINNEAPOLIS, MN 55455, USA

RECEIVED NOVEMBER 25, 2005; ACCEPTED OCTOBER 2, 2007

The evolution of melt segregation in deforming partially molten olivine-rich rocks has been studied in a series of laboratory experiments. During deformation, melt segregates into networks of anastamosing channels (or 'bands') surrounding lenses of melt-depleted material. We quantify the nature of the melt distribution in the samples, including thickness, angle, spacing, volume fraction, and melt fraction of melt-rich bands, to understand the dynamics of melt-network organization. Two series of experiments were designed to isolate the effects of (1) increasing shear strain (at similar stress levels), and (2) varying stress levels (deformed to similar shear strains). Melt-rich bands develop by a shear strain of unity. In samples deformed at varying stress levels, higher stress produces smaller characteristic band spacings. We relate these variations to the compaction length, δ_c, which varies only as a result of the reduction of matrix viscosity with increasing stress. Simple approaches to scaling from experimental to mantle conditions suggest that stress-driven melt segregation can occur in the asthenosphere; if so, it will significantly affect rheological, transport and seismic properties, with enticing consequences for our understanding of plate–mantle interactions.

KEY WORDS: *melt segregation; rock rheology; magma transport; self-organization; mid-ocean ridges*

INTRODUCTION

In the Earth, large-scale deformation is often intense in regions where melt is being produced and transported. This generalization may apply to plate boundary settings (subduction zones and mid-ocean ridges), intra-plate rifts, plume heads and boundary layers such as the D″ region and shallow asthenosphere. Deformation and melt migration are, in their own rights, complex ensembles of many processes that interact with each other in feedback relationships (e.g. Kohlstedt & Zimmerman, 1996; Kelemen *et al.*, 1997). Even in simple systems, stress causes complex behavior in the self-assembly of melts during deformation (e.g. Rosenberg & Handy, 2000; Holtzman *et al.*, 2003*a*). Considerable evidence exists for such interactions in lower crustal, and to a lesser extent, upper mantle rocks (e.g. Nicolas, 1986; Kelemen & Dick, 1995; Neves *et al.*, 1996; Vigneresse, 1999). However, the physical causes and consequences of these interactions are poorly understood and difficult to study in the field, by theory, or by experiment. We need to understand these interactions in practical and testable ways to explore their implications for the seismic, transport, and rheological properties of important volumes of the Earth.

In this study, we build on our previous studies (Holtzman *et al.*, 2003*a*, 2003*b*; Hustoft & Kohlstedt, 2006; Parsons *et al.*, 2007) in which we demonstrated that as a partially molten rock deforms at high temperatures and pressures, melt segregates spontaneously and organizes into melt-rich networks. Here, we focus on the melt distribution and the processes that control its variation in time and space. A series of experimental observations are presented to understand the dynamics of stress-driven melt segregation and its scaling relation to conditions in the Earth. Holtzman *et al.* (2003*a*) showed that stress drives melt segregation in experimental samples with compaction lengths, δ_c (Table 1), of the order of or less than the sample thickness but longer than the grain scale. This result implies that stress-driven segregation will occur in nature in any partially molten system if the compaction length is

*Corresponding author. Present address: Lamont–Doherty Earth Observatory, Columbia University, Palisades, NY 10964, USA. Fax: 612-624-3819. E-mail: benh@ldeo.columbia.edu, dlkohl@umn.edu

Table 1: List of symbols

Symbol	Meaning
σ	differential stress ($\sigma_{11} - \sigma_{33}$), MPa
τ	shear stress ($\sigma_{13} = \sigma_{12}$), MPa
γ	shear strain
$\dot{\gamma}$	shear strain rate, 1/s
$\phi_{t,b,n}$	melt fraction, total, band, non-bands
$\phi'_{b,n}$	normalized melt fraction ($\phi_{b,n}/\phi_t$, (the prime is usually dropped)
δ_c	compaction length, m
δ_{th}	thickness of bands (largest), μm
δ_{sp}, δ_l	spacing between largest bands, or thickness of lenses, μm
$a_{b,n}$	area fraction of bands (a_{bands}/a_{total})
$a'_{b,n}$	normalized area fraction ($a_{b,n}/a_t$) (the prime is usually dropped)
S_t	total segregation $= (\phi_b)(a_b)$
c	exponent in S_t parameterization (S_t^c)
α	angle of bands relative to sample shear plane, degrees
Φ	measured viscous dissipation, $= \tau\dot{\gamma}$, Pa/s
k	permeability, m^2
d	grain size, μm
η	effective shear viscosity of composite, Pa s
μ	melt viscosity, Pa s
γ_{sl}	solid–liquid interfacial energy, J/m^2
C^*	ratio of viscous stress to surface tension stress
λ	viscosity dependence on melt fraction

smaller than the spacing between any 'boundaries'. For example, in the upwelling asthenosphere beneath a ridge, δ_c is much shorter (~100–1000 m) than the width of the partially molten region (10–100 km) (Holtzman *et al.*, 2003*a*). In this study, we explore in detail the dynamics of melt segregation and deformation processes quantitatively by characterizing the properties of the melt distribution and the influence of stress and strain on these properties. Holtzman *et al.* (2005) described the effect of strain partitioning on the energetics of deformation, providing a theoretical framework with which to integrate observations from this study. Predicting the kinetics of stress-driven melt segregation will lead to a better understanding of the transport, rheological, and seismic properties of partially molten regions of the Earth.

In the Earth, melt moves from the asthenosphere to the crust or surface and, as it does, passes through many mechanical regimes, from predominantly viscous porous flow at the bottom of the melting column to flow through cracks and dikes approaching the surface (e.g. Kelemen *et al.*, 1997). Several lines of evidence suggest that mantle-derived melts, or a large portion of them, migrate upwards through chemically isolated channels in the mantle. For example, studies of active mid-ocean ridges and ophiolite complexes reveal that the uppermost mantle rocks are not in chemical equilibrium with the basaltic melts that form the overlying crust (e.g. Kelemen *et al.*, 1995, 1997). To maintain this disequilibrium, melt must move largely through chemically isolated channels or networks (e.g. Spiegelman & Kenyon, 1992). Numerous mechanisms have been proposed for such transport. Depending on the driving force for melt movement and the rheological behavior and transport properties of the peridotite host rock, melt transport in channels may be coupled to viscous flow of the solid, via processes that involve compaction (e.g. McKenzie, 1984; Scott & Stevenson, 1984; Fowler, 1990) and/or dissolution–compaction (e.g. Aharonov *et al.*, 1997). Melt transport may also occur in fractures in a solid (e.g. Nicolas, 1986; Rubin, 1998; Phipps Morgan & Holtzman, 2005), which are likely to occur in regions of the mantle with increased viscoelastic relaxation times, approaching the top of the melting region in the mantle. However, the initial stages of melt segregation, prior to transport in channels, are probably the least well understood aspect of the whole pathway. The three general classes of processes for the initial segregation of melt into channels include: (1) runaway dissolution as defined by Chadam *et al.* (1986) and applied to mantle materials (e.g. Daines & Kohlstedt, 1994; Kelemen *et al.*, 1995; Aharonov *et al.*, 1997); (2) nucleation of localized buoyancy-driven porosity waves beneath permeability barriers (e.g. Scott & Stevenson, 1984; Connolly & Podladchikov, 1998); (3) stress-driven melt segregation (e.g. Stevenson, 1989). Here, we focus on developing an understanding of (3).

Stevenson (1989) proposed a model in which deviatoric stress could drive melt segregation. In his one-dimensional (1D) pure-shear model, small variations in melt fraction cause small variations in viscosity as a result of the strong dependence of viscosity on melt fraction. These spatial variations lead to local variations in mean stress that drive melt into the weak regions, causing them to further weaken. An instability develops that continues until the melt can no longer segregate, and melt-rich bands are separated by melt-depleted regions with some characteristic spacing. Stevenson suggested that this spacing should be less than the compaction length but larger than the grain size. In an extension of a similar analysis to two dimensions, Richardson (1998) found that segregation could occur at high pure-shear strains, and had a similar limit on the preferred length scale. Hall & Parmentier (2000) sought this preferred wavelength by invoking strengthening upon dehydration of olivine during melting as a means to set a lower limit on length scale of melt segregation. Recently, a new generation of two-phase flow theory has emerged involving the physics of damage (the loss of energy in the creation of new surfaces in a deforming material), in which deformation accelerates the segregation of a fluid phase (e.g. Bercovici & Ricard, 2003). Speigelman (2003) and Rabinowicz & Vigneresse (2004),

who also solved two-phase flow equations in 2D simple shear, found that the the fastest growth is at 45°, but did not find stability of the bands at any angle. In a fully non-linear finite-difference model of the compaction equations, Katz *et al.* (2006) observed that the band angle is controlled by the stress exponent in the constitutive relation describing matrix deformation, which is stress and melt-fraction dependent. As n increases from one to six, the band angles drop from 45° to 20°. The implication of these results is that the degree of strain partitioning increases with increasing n, so band angles are reduced with increasing strain partitioning. This conclusion is conceptually similar to that reached in an analysis of the energetics of strain partitioning by Holtzman *et al.* (2005) that used only Newtonian viscosity. At present, two-phase flow theory can explain many aspects of the segregation processes observed in experiments, but many questions are open.

Numerous experimental deformation studies have been performed on partially molten rocks or analog materials in the ductile, or near-ductile regime, in compression, shear, and torsional geometries, in drained (open) and closed conditions (e.g. Dell'Angelo & Tullis, 1988; Rutter & Neumann, 1995; Zimmerman *et al.*, 1999; Rosenberg & Handy, 2000; Hirth & Kohlstedt, 2003; Mecklenburgh & Rutter, 2003; Renner *et al.*, 2003; Schmocker *et al.*, 2003; Zimmerman & Kohlstedt, 2004; Takei, 2005; Gourlay & Dahle, 2006; Hier-Majumder & Kohlstedt, 2006; Hustoft & Kohlstedt, 2006). Several of these studies have produced melt or fluid segregation similar to that observed in this study, compared in detail in the Discussion. These experiments provide theoretical models of stress-driven segregation with physical benchmarks; a nominally successful theory should be able to simulate the basic experimental observations.

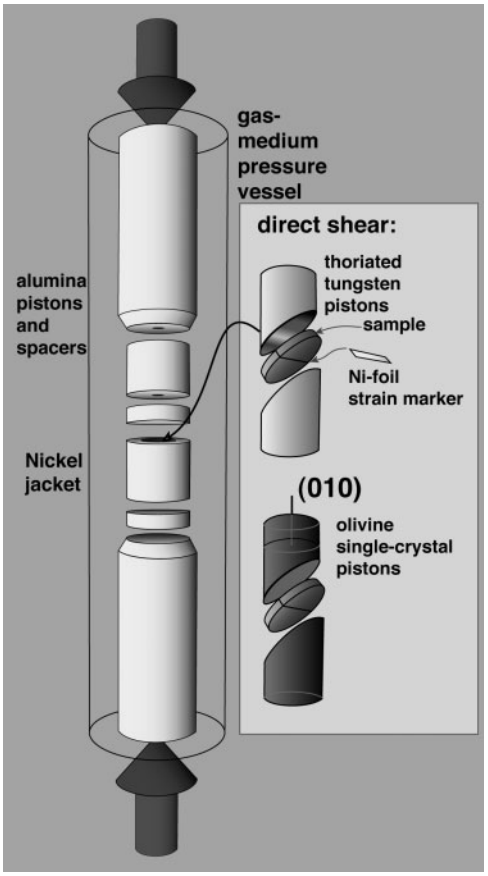

Fig. 1. Experimental apparatus. The sample assembly fits into an Fe jacket, not shown. The transparent outer cylinder represents the inner wall of the pressure vessel. The central assembly is surrounded by Ar gas at 300 MPa, which convects around the sample, providing an even temperature profile. The sample is ~1 mm thick. The other parts of the assembly are pictured roughly to scale.

EXPERIMENTAL DESIGN

The experiments were performed in a gas-medium deformation apparatus (Paterson, 1990) using a method similar to that of previous studies on olivine + mid-ocean ridge basalt (MORB) samples (e.g. Hirth & Kohlstedt, 1995*a*, 1995*b*; Kohlstedt & Zimmerman, 1996; Mei *et al.*, 2002). The materials used here are similar except for the addition of chromite to the samples, which reduces the permeability by partially blocking the pore throats between connected melt pockets, without significantly changing other physical properties of the rock (Holtzman *et al.*, 2003*a*). We performed several series of shear experiments, all at 1523 K and 300 MPa, in which melt fraction, finite strain, loading conditions, and piston type were systematically varied (Fig. 1). The melt distribution in each shear experiment was determined by image analysis.

Experimental procedure details

The starting material for all experiments reported here is composed of San Carlos olivine, chromite from the Semail Massif in the Oman ophiolite, and MORB from the Mid-Atlantic Ridge, with an olivine tholeite composition (Cooper & Kohlstedt, 1984); compositions are reported in Table 2. Olivine and chromite powders were mixed in a volume ratio of 3:1 to which MORB powders were added. The powder grain sizes were about 6 μm for olivine and 2 μm for chromite. In all cases, powders were dried at 1423 K for 8 h at an fO_2 near the Ni–NiO buffer to remove any water and then isostatically hot-pressed for 4 h at 300 MPa and 1523 K.

All experiments were performed at a confining pressure of 300 MPa and a temperature of 1523 K. The samples were placed between thoriated tungsten pistons cut at 45°, with grooves machined into them to improve gripping between sample and piston (Fig. 1), referred to as 'direct' shear experiments. This deformation geometry approximates a simple shear, but has some degree of flattening as well. One experiment (PI-902) was performed with smooth pistons made from olivine single crystals to test if

Table 2: Starting material compositions

	Olivine	Chromite	MORB
SiO_2	39·66		50·02
MgO	51·1	15	9·09
FeO	9·1	16·7	9·24
Al_2O_3	0·07	23·2	15·63
Cr_2O_3		44·2	0·05
CaO	0·14		11·51
K_2O			0·27
Na_2O	0·01		3·12
TiO_2		0·33	1·55
NiO		0·12	
MnO		0·28	

Wt % oxides in starting materials. Olivine is San Carlos olivine; chromite is from Oman ophiolite; MORB is from Mid-Atlantic Ridge.

the grooves had a significant effect on the melt distribution and band formation. Prior to deformation, some samples were cut in half normal to the shear plane and a thin piece of Ni-foil was placed between the two halves as a marker of the strain distribution in the sample.

Experiments were performed with either a constant load or a constant displacement rate applied. These boundary conditions are not exactly equivalent to constant stress or constant strain rate conditions, respectively. When a constant load is applied, the stress increases smoothly with increasing displacement because the area of contact between the pistons decreases. Constant displacement rate is much closer to a constant strain rate condition, but because the thickness of the sample decreases slightly during deformation, strain rate increases slightly. (For simplicity, we refer to them as constant strain rate experiments.) Under constant strain rate ($\dot{\gamma}$) conditions, the load varies with time in response to changes in the effective viscosity of the sample.

After deformation, samples were cut normal to the shear plane in the shear direction for image analysis. The samples were polished in colloidal silica and then etched in dilute HF–HCl solution for 10 s to aid in viewing the melt pockets. Samples were then photographed using an optical microscope with reflected light and a scanning electron microscope (SEM) with backscattered (BSE) or secondary electrons (SE). High- and low-resolution photomicrographs were used to obtain measurements of the melt distribution.

Organization of shear experiments

We investigated the effects of melt fraction, strain, and stress level on the patterns of segregation of melt and the formation of melt-rich bands. To isolate (as much as possible) the effects of these parameters, experiments are grouped into two series, summarized in Table 3. The first series focuses on the evolution of the melt distribution with progressive strain (referred to simply as the 'strain series'). The second series focused on the effect of variable stress level applied to the samples (referred to as the 'stress series'). Compaction length was varied in the strain series by varying melt fraction and in the stress series by varying the stress-sensitive solid viscosity, addressed further in the Discussion.

Strain series

The purpose of this set of experiments is to understand how the melt distribution evolves with strain or time. We systematically varied finite strain ($\gamma \sim 1$, 2, 3) keeping values of applied load similar for most experiments (except that the samples deformed to high-strain were subjected to several load levels during the experiment to obtain rheological data). These six experiments were divided into two sets, defined by their total melt fractions, $\phi_t = 0{\cdot}02$ and $\phi_t = 0{\cdot}06$, performed to observe the evolution in two systems with different values of δ_c, which depends strongly on melt fraction.

Stress series

The purpose of this series of experiments is to understand the effect of the level of stress applied to a sample on the distribution and self-organization of the melt. We deformed five samples with $\phi = 0{\cdot}04$ to the same finite strain ($\gamma \sim 3{\cdot}5$). These samples had no Ni strain marker because, in the strain series, the impermeable marker significantly altered the melt distribution and thus the dynamics of melt migration. The samples in this set were also generally thicker than those in the strain series. Three samples were deformed under constant load conditions (CL subset). Two samples were deformed under conditions of constant displacement rate (CR subset). Experiments were performed under these conditions to explore the influence of the variation of load with time (the 'loading path') on melt distribution and the evolution of rheological properties. An additional experiment was performed with a very low melt fraction, $\phi_t = 0{\cdot}005$ (PI-1070).

Methods: quantifying melt distribution

In this study we define and measure two different groups of parameters that describe properties of the melt 'configuration'. These properties include the distributions of band angles (α), spacings (δ_{sp}), thicknesses (δ_{th}), area fraction of melt bands (a_b), normalized melt content of the bands (ϕ_b) and the degree of segregation, (S_t). α, δ_{th} and δ_{sp} are the 'spatial' properties of the melt network. The other data, a_b, ϕ_b and S_t constitute the 'average' properties of the network, so called because they are effectively averaged across the sample and contain no length-scale information.

Table 3: Experimental conditions

Sample	ϕ_t	γ_f	t (h)	τ_i	τ_f	η_o	η_f	Comment
Strain series								
884	0·02	0·9	1·04	58	68	1·6e11	3·1e11	$\phi = 0{\cdot}02$ series
889	0·02	2·1	1·84	55	82	1·4e11	3·5e11	
833	0·02	3·5	1·85	56	87	1·1e11	2·1e10	
885	0·06	1·1	0·47	55	65	7·1e10	9·7e10	$\phi = 0{\cdot}06$ series
891	0·06	2·0	0·67	51	68	5·4e10	6·1e10	
830	0·06	3·0	1·50	51	76	6·1e10	7·7e10	
Stress series								
1020	0·04	3·2	6·18	28	58	1·1e11	3·9e11	low τ
1025	0·04	3·4	1·88	57	116	8·3e10	1·3e11	med τ
1027	0·04	3·7	0·59	82	177	6·6e10	3·0e10	high τ
1010	0·04	3·4	3·38	8	32	5·2e10	1·1e11	const. $\dot{\gamma}$, low τ
1096	0·04	3·4	0·91	87	65	9·1e10	6·5e10	const. $\dot{\gamma}$, high τ
Other								
1070	0·005	3·3	2·67	52	122	8·8e10	2·3e11	low ϕ
902	0·06	3·5	0·47	59	78	4·0e10	2·1e10	olivine pistons

All experiments were performed at 300 MPa confining pressure and 1523 K, subjected to constant load conditions, except for 1010 and 1096, in which there was constant displacement rate, or approximately constant $\dot{\gamma}$.

We make these distinctions to provide links to the theories used to describe these kinds of systems. The spatial properties are used for comparison with continuum two-phase flow theory. The averaged properties will be used to calculate macroscopic effective properties such as elasticity and viscosity. Thus, we want to know the relation between these two kinds of data.

Several methods of image analysis were used to measure the parameters discussed above. Length-scale data (spacing, thickness and angle) are measured directly from a 'linear intercept method' (LIM) applied to photomicrographs; others are measured with calculations performed on 1D curves of melt distribution, and some are measured with both methods, as discussed below and in Appendix A, and shown in Fig. 2. For both series of experiments, we compiled numerous reflected-light images from each sample. We analyzed images from locations with minimal influences on the distribution of melt caused by end-effects. (As will become apparent, avoiding these influences is easier in the samples without a strain marker.) To visualize only the melt, we applied a threshold to the images such that all but melt (darkest grey values) was eliminated, resulting in a binary image of the melt distribution. To the binary melt images, we applied a smoothing algorithm in which a circular filter matrix of radius r is convolved with the binary image, and then divided by the number of points in the smoothing tensor, as illustrated in Fig. 2b and c. The averaging radius is chosen to be about twice the average grain diameter, large enough to smooth the distribution and small enough to provide representative detail. Three lines were then extracted from each of these images (Fig. 9c and d) and operated upon, as discussed below.

Spatial quantities

α (band angle): the angle of each band relative to the shear plane is measured using the LIM (Appendix A).

δ_{th} (band thickness): the band thicknesses are measured with the LIM, at the same location as the angle, as far from a junction with another band as possible to avoid repetitive measurements.

δ_{sp} (band spacing): using the LIM, the largest bands are generally clear and we record the maximum spacing between them, normal to their orientation, from center to center, as far as possible from junctions of large bands. Using the autocorrelation method (Appendix A), this band spacing is defined as the lag associated with first maxima.

Average quantities

We define bands as any region with a greater-than-average melt fraction and lenses (or 'non-bands') as any region with less-than-average melt fraction. Then, we calculate the following.

(1) a_b (band area). The total area (in a 2D image) of melt-rich bands is defined as the area of sample that

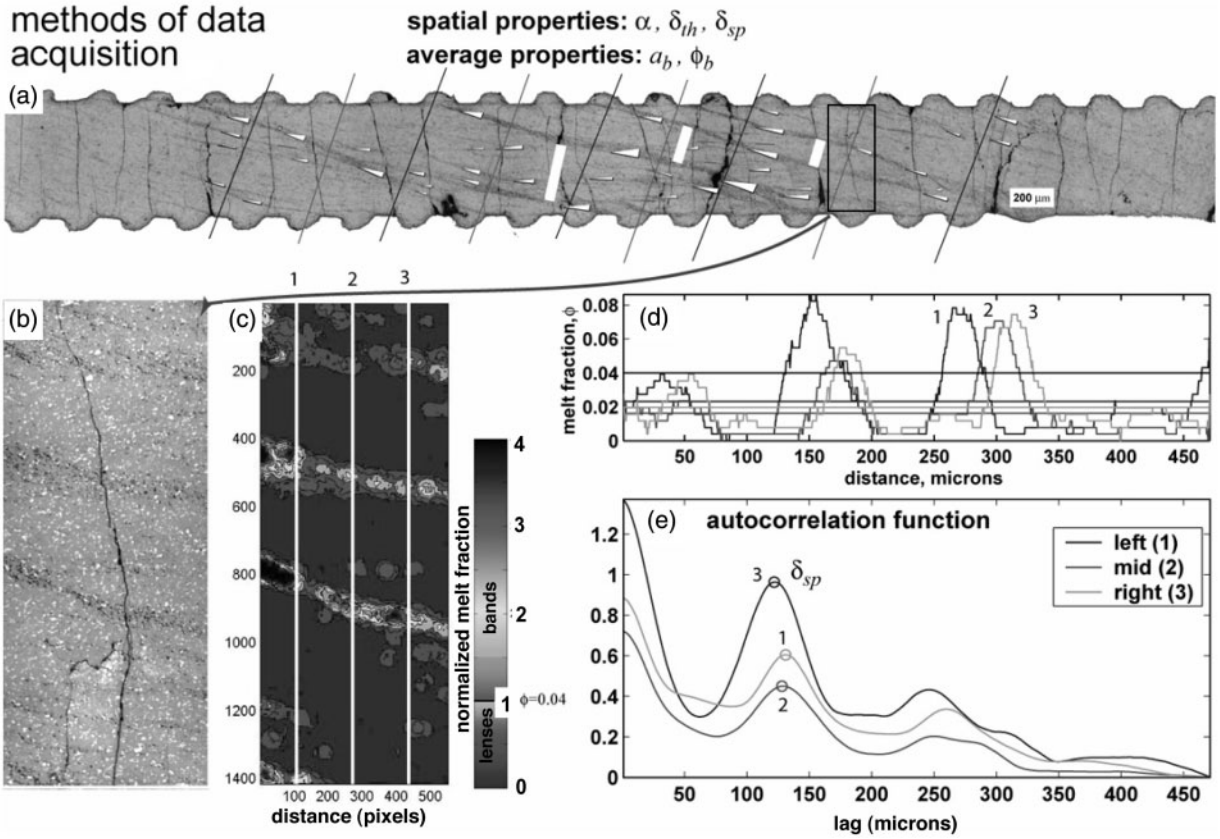

Fig. 2. Example of data acquisition method. (a) Whole sample image. Triangles represent locations where band angle and thickness data were obtained, with fine dark lines as guides for the 'linear intercept method'. The thick white lines show where band-spacing data were obtained. The locations are chosen to minimize repetition of measurements. (b) High-resolution reflected-light image spanning sample thickness from the right side of (a) indicated by the box, which is thresholded such that only melt pockets (black) remain. (c) The binary image is obtained after thresholding image (b). The result is smoothed and contoured as shown here. The three labelled linear profiles of melt fraction are analyzed as discussed in the Appendix. (d) The three linear profiles of melt fraction. The lower set of three lines shows the local average melt fraction for each line, which is, in this image, less than the total, $\phi_t = 0{\cdot}04$. (e) The autocorrelation function (ACF) for each line in (d), and the resulting value of δ_{sp}.

has a melt fraction higher than the average, divided by the total area of the sample. Actually, these measurements are made on lines, so they are 1D areas. The fractional band area, a'_b, is calculated as

$$a'_{\mathrm{b}} = \frac{a_{\mathrm{b}}}{a_{\mathrm{t}}} = \frac{\mathcal{N}^{\phi>\phi_{\mathrm{t}}}}{\mathcal{N}_{\mathrm{t}}} \tag{1}$$

in which at is the total area, $\mathcal{N}_{\mathrm{t}}$ is the total number of pixels in the 1D curve and $\mathcal{N}^{\phi>\phi_{\mathrm{t}}}$ is the number of pixels for which $\phi > \phi_{\mathrm{t}}$, calculated from the smoothed melt distribution, for which i is the 1D index. The prime indicates that the value is normalized. ϕ_{t}, where the $_{\mathrm{t}}$ indicates 'total', can be defined in two ways: first, locally

$$\phi_{\mathrm{t}}^{\mathrm{loc}} = \frac{\sum_{i=1}^{\mathcal{N}} \phi_i}{\mathcal{N}_{\mathrm{t}}} \tag{2}$$

or, second, prescribed as being constant for all lines from a sample. The ϕ_{t} value is fixed as that volume fraction of MORB put into the sample. (For each line of data, $\phi_{\mathrm{t}}^{\mathrm{loc}}$ is calculated as well.) a_{b} is calculated locally for each line of data; the area fraction of the lenses, a_{n}, is calculated in an analogous manner.

(2) ϕ_{b} ('normalized band melt fraction'). The average melt fraction in the bands, ϕ_{b}, is the sum of the melt fraction values at every point in the band, divided by the number of points in the band:

$$\phi'_{\mathrm{b}} = \frac{\phi_{\mathrm{b}}}{\phi_{\mathrm{t}}} = \frac{\sum_{i=1}^{\mathcal{N}} \phi_i^{\phi>\phi_{\mathrm{t}}}}{\mathcal{N}^{\phi>\phi_{\mathrm{t}}}\phi_{\mathrm{t}}} \tag{3}$$

which of course depends on the value of ϕ_{t} used, as discussed above. In all data presented here, we use the global ϕ_{t} fixed for each sample. ϕ'_{n} is calculated in the same manner.

Mass balance can be written in terms of these parameters; a_b, a_n, ϕ_b, and ϕ_n must be related within one line as follows:

$$a_b\phi_b + a_n\phi_n = a_t\phi_t. \quad (4)$$

Normalizing by $a_t\phi_t$, we obtain

$$a'_b\phi'_b + a'_n\phi'_n = 1. \quad (5)$$

The segregation factor, S_t

As a deforming system evolves with increasing strain, the melt will progressively segregate. However, we will never be able to measure strain directly in partially molten mantle. The best we can hope for is to measure some physical property that is related to the degree of melt segregation. Here we introduce a new parameter, S_t. S_t is a scalar measure of the degree of melt segregation, defined as

$$S_t = a'_b\phi'_b = \frac{a_b}{a_t}\frac{\phi_b}{\phi_t^{global}} = 1 - a'_n\phi'_n. \quad (6)$$

When $S_t = 0$, melt is homogeneously distributed; when $S_t = 1$, all the melt is segregated into networks. Because we need to know a'_b and ϕ'_b to estimate seismic properties (Holtzman & Kendall, in preparation) and effective viscosity (Holtzman *et al.*, 2005), but cannot measure them independently in the Earth, we would like to constrain the relation between a'_b and ϕ'_b. (In the sense that S_t reflects the degree of order in the system, it can also be seen as an inverse measure of configurational entropy, S; the higher the value of S_t, the lower the value of S).

In a closed system, S_t must be between zero and unity, when measured over the volume of the sample. However, if melt flows into or out of the system, then any given cross-section can contain more or less than the average melt fraction such that $S_t > 1$ or $S_t < 1$, respectively, even if all the melt appears to be segregated. This accounting problem can occur when S_t is measured in only one plane (or part) of a sample, as is done in this study. To account for flow into or out of the plane of measurement (or in nature, an open system), we can normalize by the local total melt fraction (the melt fraction in the line or area of measurement),

$$S_t^{local} = a'_b\left(\frac{\phi_b}{\phi_t^{local}}\right) \quad (7)$$

where $\phi_t^{local} = a'_b\phi_b + a'_n\phi_n$ for a 2D section. Therefore,

$$S_t^{local} = a'_b\left(\frac{a'_b\phi_b}{a'_b\phi_b + a'_n\phi_n}\right). \quad (8)$$

It should be noted also that

$$S_t^{local} = \frac{a'_b\phi_b}{\phi_t^{local}}\left(\frac{\phi_t^{glocal}}{\phi_t^{local}}\right) = S_t\left(\frac{\phi_t^{glocal}}{\phi_t^{local}}\right). \quad (9)$$

This equation is useful because it relates the local and global values of S_t with a single scalar, the ratio of the global to local melt fractions. It is also necessary to adjust the values of a'_b and ϕ'_b, as demonstrated below. However, it is not obvious how to split the weighting between a'_b and ϕ'_b. For now, until the physics is better understood, we use the following expression:

$$S_t^{local} = \left(\sqrt{\frac{\phi_t^{glocal}}{\phi_t^{local}}}a'_b\right)\left(\sqrt{\frac{\phi_t^{glocal}}{\phi_t^{local}}}\phi'_b\right). \quad (10)$$

S_t does not uniquely describe the evolution of the melt configuration, but we can define various paths of a'_b and ϕ'_b in terms of S_t. From experimental observations, we know that a'_b and ϕ'_b increase with increasing strain. The following equations, although empirical, adhere to mass balance (Holtzman *et al.*, 2005):

$$\phi'_b = 1 + (\phi'_{max} - 1)(S_t)^c \quad (11)$$

and by definition,

$$a'_b = \frac{S_t}{\phi'_b} = \frac{S_t}{1 + (\phi'_{max} - 1)(S_t)^c}. \quad (12)$$

The constants c, a'_{max} and ϕ'_{max} are determined by fitting these functions to the experimental data. They describe possible relationships between the measured parameters and S_t. Hereon, we drop the primes on ϕ'_b and a'_b.

RESULTS

Starting materials

As shown in Fig. 3, the starting material is a homogeneous and isotropic distribution of olivine, chromite and basaltic melt–glass. The olivine grains grew during the 4 h hot-presses from an initial mean grain size of 6 μm to a final mean grain size of 8 μm. (The grains grew to about 10 μm during the shear experiments.) The chromite has a mean grain size of 3 μm (slightly smaller in the stress series). Small chromite grains (<1 μm) are incorporated within olivine crystals and larger ones (>1 μm) are located in three- and four-grain junctions, surrounded by melt. The melt distribution is heterogeneous at the local length scale of several times the grain diameter, but roughly homogeneous at longer length scales (i.e. bands do not exist in the hot-pressed starting material). The volume fractions of melt in the starting materials are close to the volume fractions of MORB added, $\phi_t = 0{\cdot}02 \pm 0{\cdot}01$ and $\phi_t = 0{\cdot}06 \pm 0{\cdot}01$ for the strain series and $\phi_t = 0{\cdot}04 \pm 0{\cdot}01$ for the stress series.

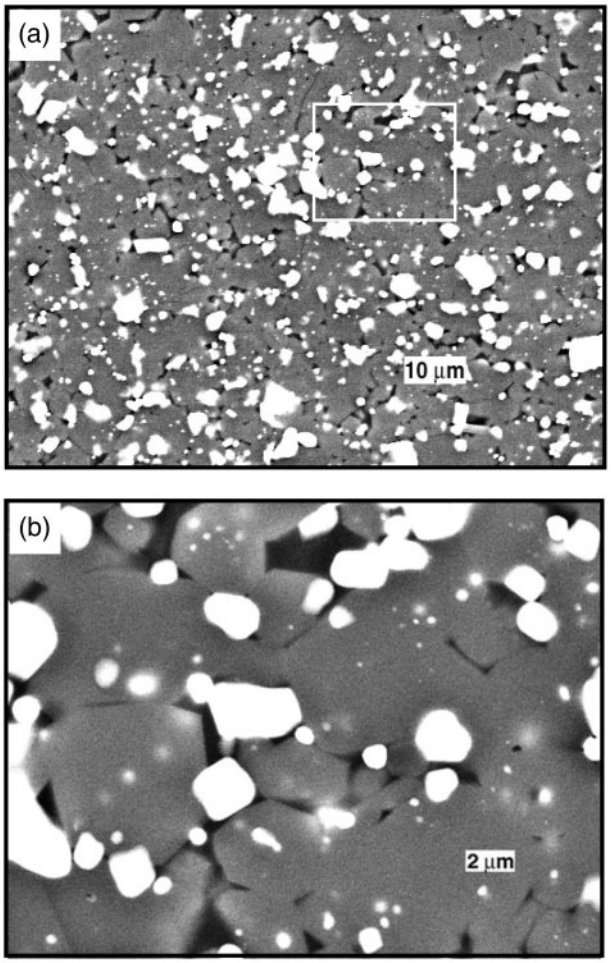

Fig. 3. SEM (BSE) images of the starting material, $\Phi_t = 0{\cdot}06$ MORB. The white phase is chromite, the grey is olivine, and the dark intracrystalline phase is basaltic glass. It should be noted that there are many sub-micron grains of chromite included in the olivine grains. In the deformed samples, many of these small grains have disappeared, possibly as a result of recrystallization of olivine grains, liberation of small chromite grains to grain boundaries, and consumption of small chromite grains by growth of larger ones. The white box in (a) is expanded in (b).

Strain series

Here, we present the detailed observations of the first set of shear experiments, focused on the evolution of melt segregation with increasing shear strain. The data come in several forms, visual and quantitative, including (1) images of the melt distribution across the entire sample and (2) distributions of band angles, thicknesses and spacings.

In Fig. 4, the evolution of melt segregation in two series is shown, grouped by average melt fraction ($\phi_t = 0{\cdot}02$ and $\phi_t = 0{\cdot}06$) and increasing finite strain. In the $\phi_t = 0{\cdot}02$ series, bands are well developed by $\gamma \sim 1$; in the $\phi_t = 0{\cdot}06$ series, bands are barely developed by $\gamma \sim 1$ but are well developed by $\gamma \sim 2$. Melt segregates first into narrow, closely spaced bands (PI-884 and PI-885). The thickness and spacing of these bands increases with increasing strain, as demonstrated by more quantitative measures presented below. It is not possible to tell from these experiments if the melt configuration has reached a dynamic steady state by $\gamma \sim 3{\cdot}5$ because the sample thickness (but not volume) is decreasing and melt is constantly rearranging itself in response to these changes.

Two boundary effects influence the organization of the bands: the pressure variations at the ends of the sample and the permeability variations associated with the strain marker at the center of the sample. The main end effect is due to low-pressure focal points at the ends of each sample where the Ni jacket meets the sample and the piston. The number of bands and quantity of melt increases toward these focal points (Fig. 4). Further towards the ends of the sample from these points, the sample is supported only by the Ni jacket, and thus the mean stress is significantly lower. Melt does not appear to flow past the point into the ends of the sample supported by the Ni jacket.

The second major influence on the network geometry in these experiments is the essentially impermeable Ni strain marker. In general, the melt fraction decreases around the strain marker, presumably because the melt is drawn away by the network, towards the low-pressure points. At the rare locations where melt bands cross the strain marker, an offset on the strain marker (but not necessarily a discontinuity) is well developed. At locations where there is offset but no band, the offset probably represents the previous location of a band that has since moved elsewhere.

High-resolution (SEM) images of melt-rich bands

In this section, detailed views of one experimental sample (PI-902) are shown to illustrate the range of microstructures in the bands. This sample, with $\phi_t = 0{\cdot}06$, was deformed to a shear strain of $\gamma = 3{\cdot}5$ using groove-free pistons made from olivine single crystals. Groove-free pistons were used to eliminate the possibility that the segregation is caused by pressure gradients associated with the grooves (and that the band spacing and network morphology are determined by the groove spacing). The single-crystal pistons were oriented with [010] normal or parallel to the compression direction, minimizing the resolved shear stress on the easy slip system. The pistons did not appear to deform. During deformation, melt segregated strongly into bands, as shown in Fig. 5a–e.

The image of the whole sample in Fig. 5a reveals well-developed bands on both sides of the strain marker. At higher magnification, Fig. 5b illustrates that some of the bands span the thickness of the sample, whereas others terminate in the middle. The bands have an average angle of $16{\cdot}4 \pm 6{\cdot}9^\circ$ with respect to the shear plane. The average amount of melt in the bands in this sample is $\phi_b = 0{\cdot}10$ (not normalized); in the melt-depleted lenses, $\phi_n = 0{\cdot}02$.

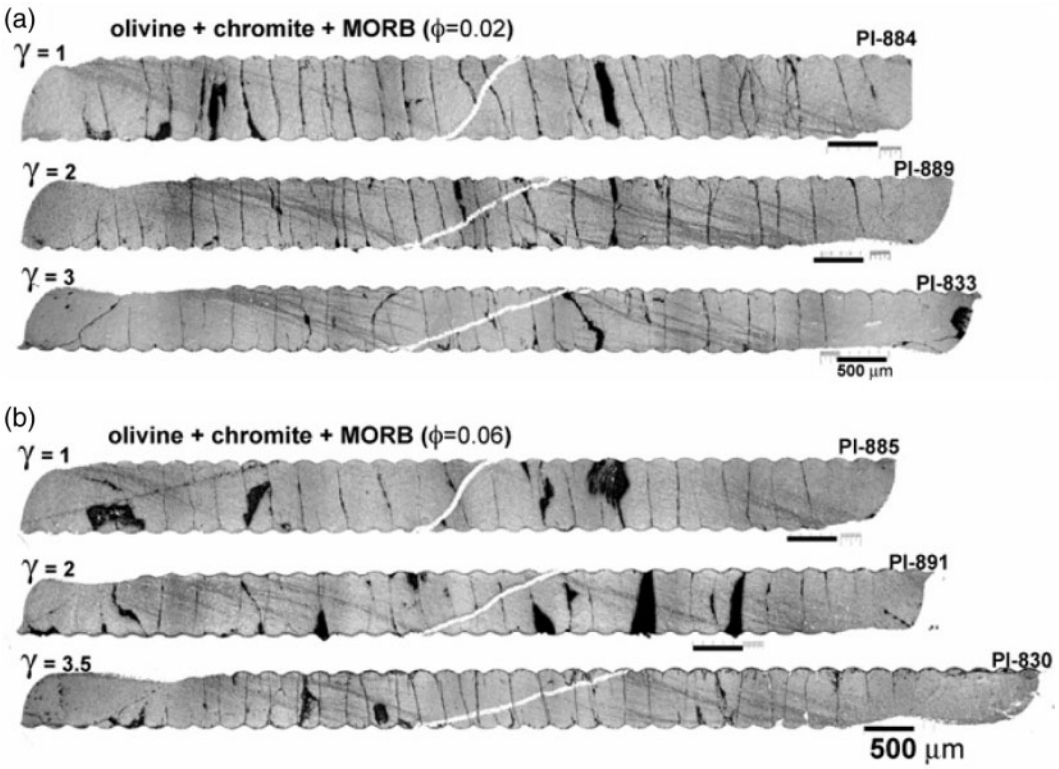

Fig. 4. Reflected-light optical images of samples in the 'strain series', deformed top-to-the-right, the x–z plane (where z is normal to the shear plane x–y, and x is parallel to the shear direction). In all images, the vertical black lines are cracks created during the quenching of the sample; the white lines are the Ni strain marker; the grey lines are the melt-rich bands. The groove spacing is 250 μm. (a) Samples with $\phi = 0{\cdot}02$ were sheared to $\gamma = 1$, 2 and 3. (b) Samples with $\phi = 0{\cdot}06$ were sheared to $\gamma = 1$, 2 and 3·5.

In Fig. 5c, a band at lower angle appears to connect two bands at higher angles. The observation that narrow bands occur at lower angles than wider bands appears in all samples.

A higher magnification view of one band in Fig. 5d reveals several interesting features. First, in some places, the edges of the band are very well defined, marked by a dramatic change in melt fraction; in other regions, the transition from band- to non-band regions are more gradational. Furthermore, inside the band, variations in melt fraction are large, with islands of low melt fraction surrounded by melt-rich channels. In other words, a larger band may be viewed as a cluster of smaller bands. In Fig. 5d and e, it is clear that the melt fraction can be locally very high in a band. As annotated in the images, the olivine crystals in the bands appear to be both dissolving and growing by precipitation, as suggested by the presence of very small grains (<1 μm), incised or corrugated grain boundaries of the large grains and the highly euhedral overgrowths on olivine grains, respectively.

Melt configuration statistics

The frequency distributions of band angles, thicknesses, and spacings are presented here (Table 4). The band angles in each sample have normal distributions, as shown in Fig. 6. As a function of strain, the band angles appear remarkably constant, at $20 \pm 6^\circ$ in the $\phi_t = 0{\cdot}02$ set and $17 \pm 6^\circ$ in the $\phi_t = 0{\cdot}06$ set. The angles increase slightly with increasing strain in the $\phi_t = 0{\cdot}02$ set but not in the $\phi_t = 0{\cdot}06$ set, as shown in the top right box of Fig. 6. Bands were not clearly visible in most of the sample with $\phi_t = 0{\cdot}06$ deformed to $\gamma = 1{\cdot}1$ (PI-885), so no data exist for low strain at $\phi_t = 0{\cdot}06$ in Figs. 6–8.

In contrast to the distribution of angles, the statistical distributions of the band thicknesses are clearly not normal distributions; in log–log space (upper right corner of Fig. 7), the distribution appears to follow a power law, $n_{th} \propto \delta_{th}^{-m}$, where n_{th} is the frequency of occurrence of a given thickness of a band of thickness, δ_{th}, where the mean value of m is 1·7 (values for each sample are listed in Fig. 7). We cannot test the robustness of the apparent power-law nature of this distribution because the thickness data only span up to one order of magnitude. In the images in Fig. 4, the thicknesses of the bands appears to increase between $\gamma = 1$ and $\gamma = 2$ in both the $\phi_t = 0{\cdot}02$ and $\phi_t = 0{\cdot}06$ series, but there does not appear to be a systematic difference between the data from samples deformed to $\gamma \sim 2$ and $\gamma \sim 3$. These visual inferences appear in the

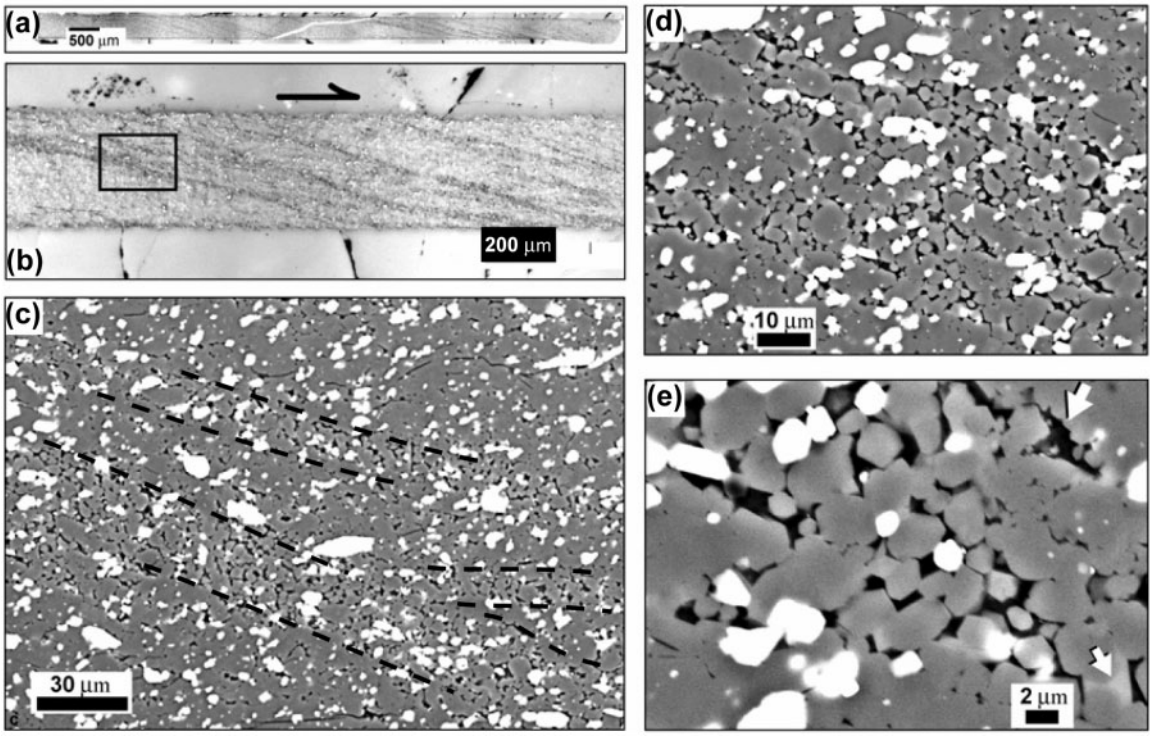

Fig. 5. Images of a sample (PI-902) with $\phi = 0{\cdot}06$ MORB, deformed to a shear strain of $\gamma = 3{\cdot}5$ using groove-free pistons made of olivine single crystals. (a) Reflected-light optical micrograph of whole sample. Unlike the samples deformed using tungsten pistons, the sample did not crack during the quench. The Ni strain marker is the white band extending NE–SW. (b) Reflected light optical micrograph of the right side of the sample. The melt-rich bands appear as dark grey streaks trending NW–SE. (c) SEM-BSE image of two parallel bands oriented $\sim 20^\circ$ to the shear plane, outlined with dashes. It should be noted that a third narrower band exists at a lower angle in the bottom right corner. The implications of this often-observed geometry of high- and low-angle bands are discussed in the text. (d) SEM-BSE image of one band. The general alignment of melt-rich pockets at a low angle ($\sim 10^\circ$) to the wall of the bands, the local shear plane, should be noted. (e) SEM-BSE image of the edge of a band shown in (d). In the upper right, the corroded grain boundaries and very small euhedral grains (<1 μm), marked by an arrow, should be noted. These grains may be produced by crystallization and/or by melt corroding subgrain walls in larger crystals. In the lower right, the lighter grey solid between the darker olivine grains should be noted. This phase may be clinopyroxene or Ca-rich olivine precipitated rapidly. Olivine crystals in the bands appear to be both dissolving and growing by precipitation in close proximity, as suggested by the presence of very small grains, incised or corrugated grain boundaries of the large grain and the euhedral overgrowths of olivine grains, respectively.

histograms in the high-end tails of the distribution, but do not appear in the mean values, as shown in Fig. 9a.

A correlation was found between the band angle and band thickness, as shown in Fig. 8. The correlation coefficients (R^2), shown in Fig. 8, decrease slightly with increasing strain. In the samples deformed to higher strain ($\gamma = 2$–$3{\cdot}5$), the trends appear to reach a cap at an angle of $\sim 30^\circ$, but the thicknesses simply increase with increasing strain whereas the bands appear unable to rotate past this angle. This correlation is the statistical expression of an anastomosing network of bands, as observed in the photomicrographs.

The spacings between the largest bands, δ_{sp}, were measured with both LIM and the autocorrelation function (ACF) for all samples. The results of both methods are plotted as a function of γ in Fig. 9. The data show essentially that the band spacings increase only slightly with increasing strain for both series of initial melt fractions, although uncertainties are larger than observed variations. For the high-strain samples, the measurements of δ_{sp} data from LIM and ACF methods are consistent. In general, the average value of δ_{sp} increases with increasing strain (except for the drop in δ_{sp} in the high-strain sample in the $\phi_t = 0{\cdot}02$ set, as shown in Fig. 9). To what extent the average spacing in band networks will reach a steady state with increasing time or strain cannot be determined from this set of experiments, but broadly speaking, the melt distribution does not evolve dramatically after $\gamma = 1$.

Summary

(1) The band angles have normal distributions with a mean of $\sim 20^\circ$. The mean values of both sets appear to be independent of strain (Fig. 6).
(2) Band thicknesses do not have normal distributions; they appear to have a power-law distribution, but the data are limited to less than one order of magnitude of length scale. The thickness of the thickest bands, but

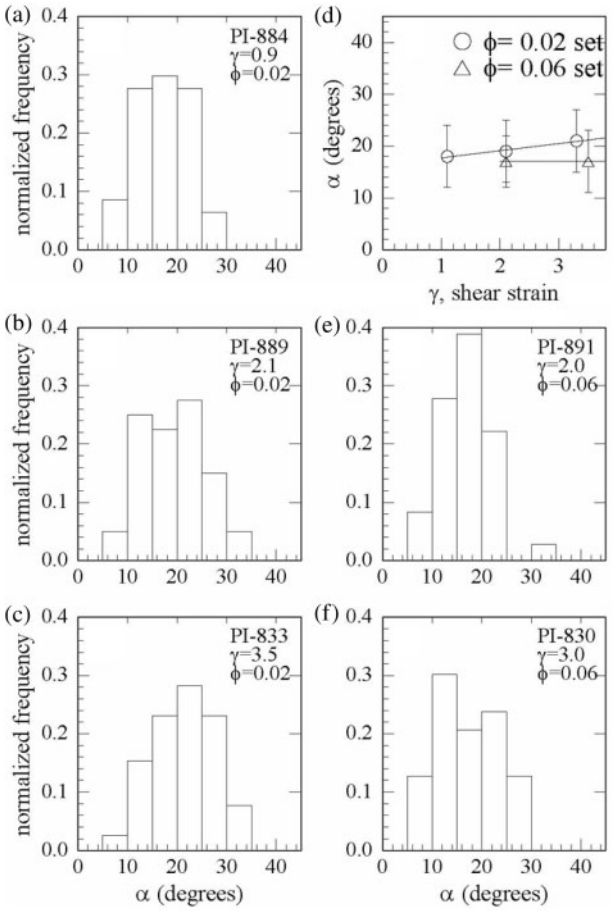

Fig. 6. Histograms of band angles, α, for the $\phi = 0{\cdot}02$ (a–c) and $\phi = 0{\cdot}06$ (e and f) sets in the strain series. Strain increases downward. The lower strain experiment in the $\phi = 0{\cdot}06$ set did not develop bands that were distinct enough to apply the linear intercept method. (d) Mean and standard deviation of the α distributions as a function of shear strain, γ.

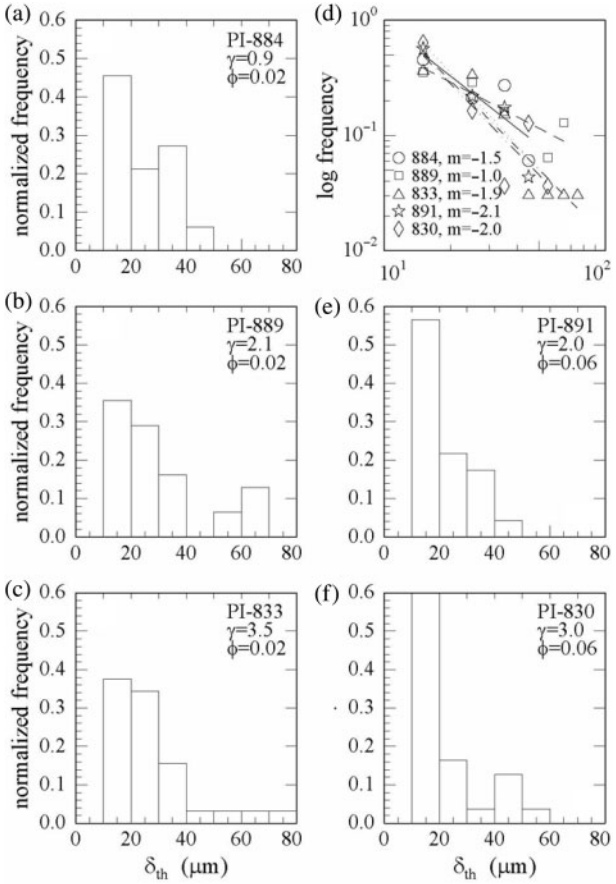

Fig. 7. Histograms of band thicknesses, δ_{th}, for samples with $\phi = 0{\cdot}02$ (a–c) and $\phi = 0{\cdot}06$ (e and f) in the strain series. Strain increases downward. The low-strain experiment in the $\phi = 0{\cdot}06$ series (PI-885) did not develop melt-rich bands distinct enough to apply the linear intercept method. (d) Histograms of δ_{th} in log–log space for the five samples (a–c, e and f), to illustrate the crude power-law distribution, with slopes *m* listed in the legend.

not the mean thickness, appears to increase with increasing strain (Fig. 7).

(3) A positive correlation exists between band thickness and band angle; the increase in band angle with increasing band thickness is roughly linear, with a slight upturn to higher thicknesses at an upper limit of angle of $\sim 30^\circ$ (Fig. 8).

(4) The spacing between large bands increases with increasing strain up to $\gamma \sim 2$. This trend appears clearly in the reflected-light images and Fig. 9.

The most robust observation is simply that by a shear strain of $\gamma \sim 1$, the melt has begun to segregate into clear networks; by a shear strain of $\gamma \sim 2$, the networks are well developed. However, there are noticeable differences in the two subsets of experiments with different average melt fractions ($\phi_t = 0{\cdot}02$ and $\phi_t = 0{\cdot}06$). Melt segregation is more advanced at a shear strain of $\gamma \sim 1$ in the set with $\phi_t = 0{\cdot}02$ than in the set with $\phi_t = 0{\cdot}06$. However, as a function of time, the networks develop more quickly in the $\phi_t = 0{\cdot}06$ set. Because the applied stresses were similar in the two sets (Table 2), the quicker segregation in the samples with higher melt fraction was probably due to lower resistance to melt migration (increased permeability and decreased composite viscosity).

The primary problem with the above datasets is that the network quickly finds its physical constraints, which are created by the low-pressure end-points of the piston and the impermeable strain marker in the middle. Because these two constraints impose such tight restrictions on the organization of the melt, we found that the statistical measures of the band area and average melt fraction (Table 6), and to some extent spacings and thickness, are difficult to interpret. We hesitate to probe too deeply into the details of the band networks and and their scaling properties. With

so little room in which the melt can organize, the spacings and average properties of the melt distribution at large strains are probably controlled more by the boundary conditions (the proximity of the piston–sample interfaces) than the thermodynamic state. To remove as many of these complications as possible, we eliminated the strain marker in subsequent shear experiments.

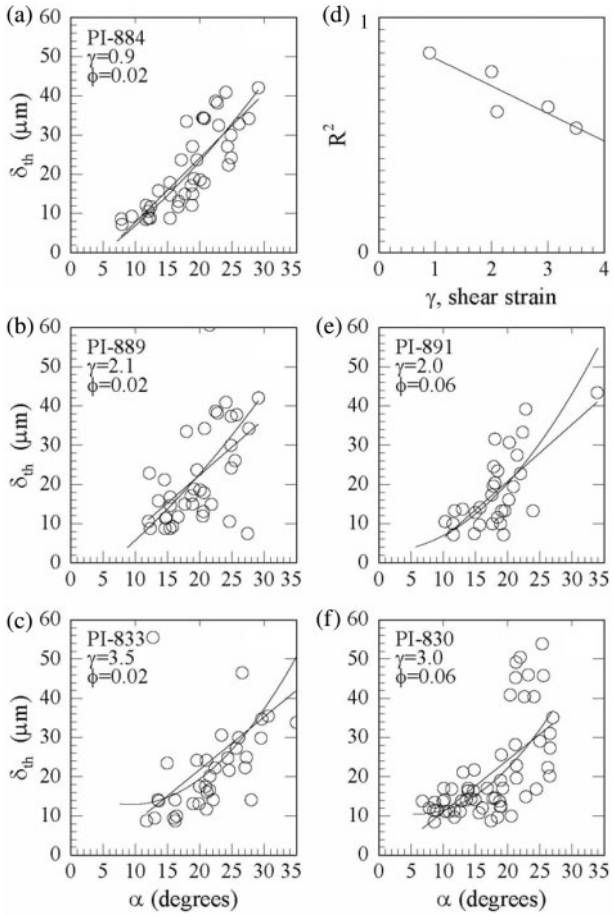

Fig. 8. Correlations of band thicknesses, δ_{th}, and angles, α for samples with $\phi = 0{\cdot}02$ (a–c) and $\phi = 0{\cdot}06$ (e and f). Strain increases downward. The data were fitted with a linear best fit and a second-order polynomial. (d) R^2 as a function of shear strain.

Stress series

The major improvements in the method from the strain series experiments are the removal of the strain marker and an increase in the sample thickness, both of which give the melt-rich networks more space in which to organize. The networks are much better developed because of the reduction in spatial constraints on their organization. The three experiments performed at constant, but different, load conditions are referred to as the 'constant load' (CL) subset; the two experiments performed under constant displacement rate conditions, which approximates constant strain rate, are referred to as the constant strain or displacement rate (CR) subset.

Images

In the images of the three samples of the CL set (Fig. 10) and the two samples of the CR set (Fig. 11), the effect of stress on the melt distribution is clear. In the CL set, with increasing stress, the bands become narrower and more closely spaced. In the CR set, with increasing strain rate (also increasing stress), the bands also become narrower and more closely spaced, although the differences are more subtle. The morphology of the band networks also depends on the stress level. The bands become straighter and the junctions more angular with increasing stress, as seen by comparing Fig. 10a and c. The same anastomosing patterns of narrow low-angle bands and wider higher-angle bands exist in these samples as in the strain series. The anastomosing patterns are more penetrative and have a finer scale at high stress than at low stress.

The anastomosing pattern is three dimensional. In Fig. 12, two orthogonal reflected-light images of sample PI-1025 are shown in perspective, to give a sense of the 3D

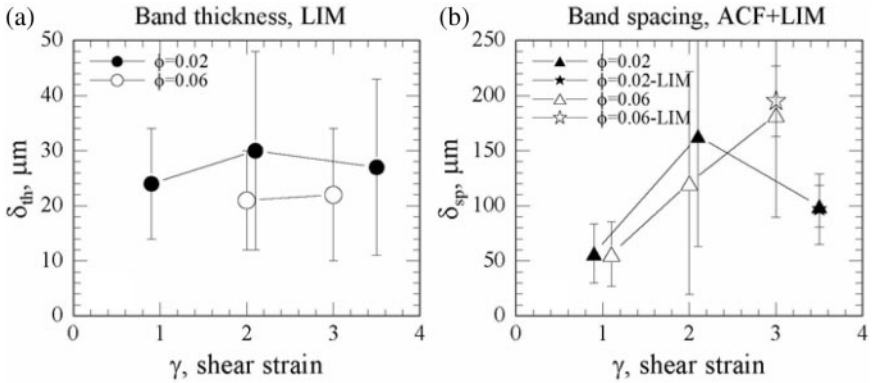

Fig. 9. (a) Band thickness data determined by the linear intercept method (LIM), plotted as a function of shear strain. (b) Band spacing data determined by the autocorrelation function and LIM, plotted as a function of shear strain.

nature of the melt-rich networks. As indicated in the schematic drawing of 3D networks from Holtzman *et al.* (2003*b*), the average length of lenses is greater in the plane normal to the shear direction than it is in the flow plane (the usual view). Also, some sample material has been extruded laterally (in the shear plane, normal to the shear direction) beyond the edges of the piston. It also appears that the melt fraction is higher in and near this extruded material, indicating that there may be some flux of melt from the middle of the sample towards the edges.

The visual and statistical signature of the anastomosing networks is a bimodal distribution of band angles, as illustrated in Fig. 13. In this image, and in all of the samples, there are indications of some scale-invariant properties of the distribution of melt. The first-order structure is the largest bands, which are oriented at $\alpha \sim 15$–25° to the sample shear plane (that is, the grooved piston surface) in Fig. 13c. The population of smaller bands, the second-order structures, is oriented at $\alpha \sim 5$–15° to the sample shear plane. However, if one views these structures in a local reference frame of the lenses, such that the shear plane in the lenses is back-rotated by $\sim 10^\circ$ to the sample shear plane (the piston surface), then the secondary bands are oriented at $\alpha \sim 15$–25° with respect to this secondary shear plane, illustrated in Fig. 13c. In other words, the secondary narrow bands that cut across lenses are controlled by the local stress field in the lenses. This local rotation of the stress field in the lenses is suggested by the back-rotation of olivine *b*-planes (Holtzman *et al.*, 2003*b*) and by the analysis of strain partitioning (Holtzman *et al.*, 2005). Extending this point of view one order downward in scale, the melt pockets most visible in the large bands are also oriented $\sim 20^\circ$ to the wall of the band, the third-order shear plane defined by the surfaces of the melt bands. Thus, from the sample scale to the grain scale, there are three levels of scale-invariance to the orientation of melt alignment relative to the local and applied stress tensors.

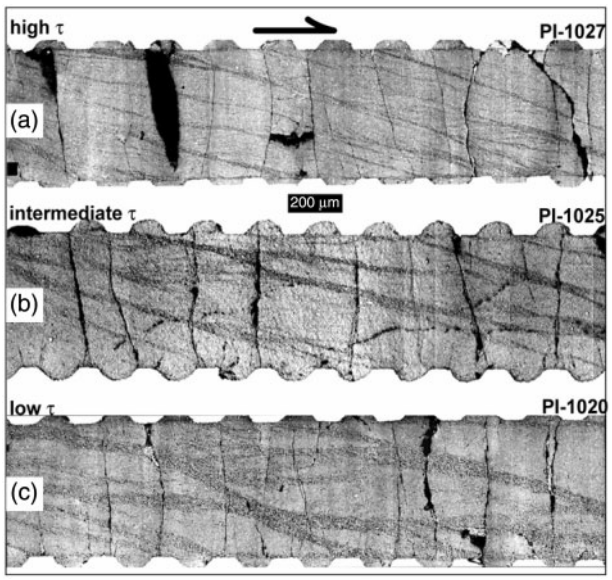

Fig. 10. Reflected light images samples (a) PI-1027, (b) PI-1025, and (b) PI-1020, in the stress series, sheared at constant load, top-to-the-right, decreasing in applied load from (a) to (c). As with the previous strain series, the vertical black cracks are caused by quenching the sample at the end of an experimental run and should be ignored. The groove spacing is 250 μm and the melt-rich bands are the darker grey channels aligned at about 15° to the shear plane.

Is there a lower limit to the melt fraction required for segregation to occur? The sample with $\phi = 0{\cdot}005$ was deformed at moderate stresses ($\tau_f = 122$ MPa). Well-defined bands formed, as shown in detail in Fig. 14. The bands are narrow and the lenses between them have almost no visible melt. Furthermore, the chromite grains in the lenses appear to be stretched and aligned, forming an apparent foliation. However, where a band is present, the chromite grains are larger, fewer and less elongated, as shown in Fig. 14. This pattern suggests that chromite grain growth (an Ostwald ripening process) is much more efficient in the presence of melt than in its absence. These variations in chromite morphology are not present (or nearly as clearly) in samples with more melt, suggesting that the presence of melt significantly enhances chromite grain growth.

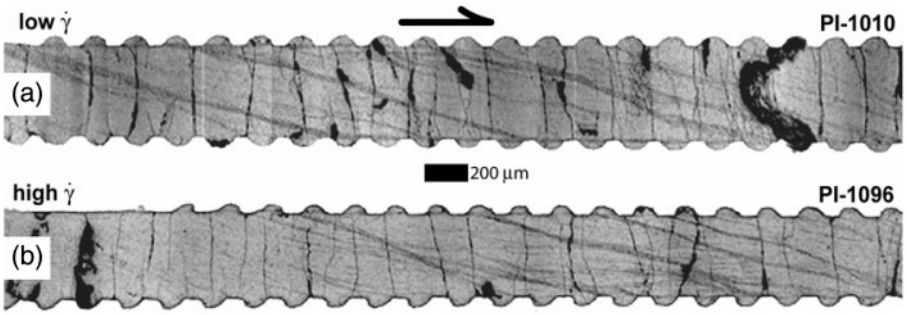

Fig. 11. Reflected light images of samples sheared under constant displacement rate conditions (that approximate constant strain rate) of (a) $3 \times 10^{-4}\,s^{-1}$ and (b) $1 \times 10^{-3}\,s^{-1}$.

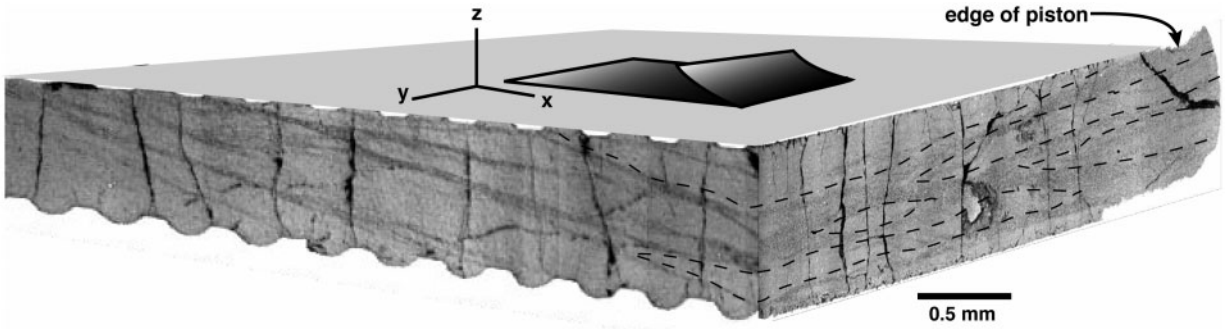

Fig. 12. Three-dimensional view of sample PI-1025. The melt-depleted lenses (outlined with dashes) are generally longer in the direction normal to shear (y) than parallel to shear (x), consistent with the olivine a-axis alignment discussed by Holtzman *et al.* (2003*b*, fig. 3). The sample extruded outwards beyond the edge of the piston, as marked by the arrow.

Melt configuration statistics

Below, we characterize the details of these various melt distribution parameters (Table 5) and plot each of them as functions of stress (the shear stress at the end of the experiment, τ_f) and time, to develop the hypothesis that some of these parameters are controlled by thermodynamics (stress) and some by kinetics (time). Again, the question remains as to whether or not these band systems achieve a steady state.

The distributions of band angles in this series of experiments, shown in Fig. 15, have different patterns from those in the strain series of experiments. In almost all samples (except for PI-1010), the distributions are bimodal, and within each population, the distributions look asymmetric, not Gaussian (however, there are too few data and too few decades of length scale to suppose a power-law distribution). However, as shown in the upper right-hand plot in Fig. 15, the distributions of angles (from the higher angle subset of the bimodal distribution) have very consistent mean values of $\sim 18^\circ$, independent of stress (or strain or time), similar to the mean of the strain series experiments.

The distributions of band thicknesses, δ_{th}, in Fig. 16, also appear to have asymmetric and possibly power-law distributions. The mean values decrease as a function of increasing stress. The distribution of δ_{th} in PI-1020 is the one exception, with no clear asymmetry. Interestingly, there is a clear difference in mean values between the CL and CR sets: the constant strain rate experiments tend to have narrower bands, even for the same value of τ_f.

The correlation between α and δ_{th} that was clear in the strain series experiments is not well defined in this series, as shown in Fig. 17. The correlation coefficients, R^2, for each sample in both series, plotted in the upper right-hand corner of Fig. 17, show an increase with increasing stress, but also demonstrate low values relative to the strain series (whose values are also independent of stress). This decrease in R^2 in the stress series relative to the strain series may occur because the angles have a more clearly bimodal distribution than the thicknesses do and because the networks are less constrained spatially and thus have more variability. The most ubiquitous and significant feature of these distributions is that α does not exceed $\sim 25^\circ$.

Because the samples are larger and the networks more continuous in the stress series than in the strain series, the statistics on spatial properties in the system are of better quality. In general, both δ_{th} and δ_{sp} decrease with increasing stress, as shown in Fig. 18a and b respectively, in accordance with the visual observations. The δ_{sp} vs τ data appear to collapse onto one trend as a function of stress, as shown in Fig. 18b. For δ_{sp}, the agreement between the ACF and the LIM data is fairly good, except for one sample (PI-1096). When plotted against time, the mean values of δ_{sp} for both the CL and CR series increase with increasing time, but the data from the two sets do not collapse onto one line. Thus, it appears that δ_{sp} is controlled by stress, and it does not depend a great deal on the loading path or stress or strain history.

Interestingly, the δ_{th} vs time data seem to collapse onto one line, much more so than the δ_{th} vs τ data, as shown in comparison of Fig. 18a and c. The implication of this observation is that the thickness has not reached steady state.

In Fig. 19, the average properties of the melt distribution (a_b, ϕ_b, Table 7) are plotted as functions of shear stress and time. All values appear to decrease with increasing stress (Fig. 19a) and increase with increasing time (Fig. 19b). As functions of shear stress, all values are systematically lower in the CR series than in the CL series. However, when plotted as a function of time, the data appear to collapse onto single lines, suggesting that the average properties of the melt distribution have not reached steady state (similar to δ_{th} but not δ_{sp}).

There are limitations to how far we can interpret stress control (steady state) vs kinetically limited (non-steady state) for these various parameters. One way of determining whether a sample is in steady state is to look at rheological data, shown in Fig. 20. In the CL set, the stress always

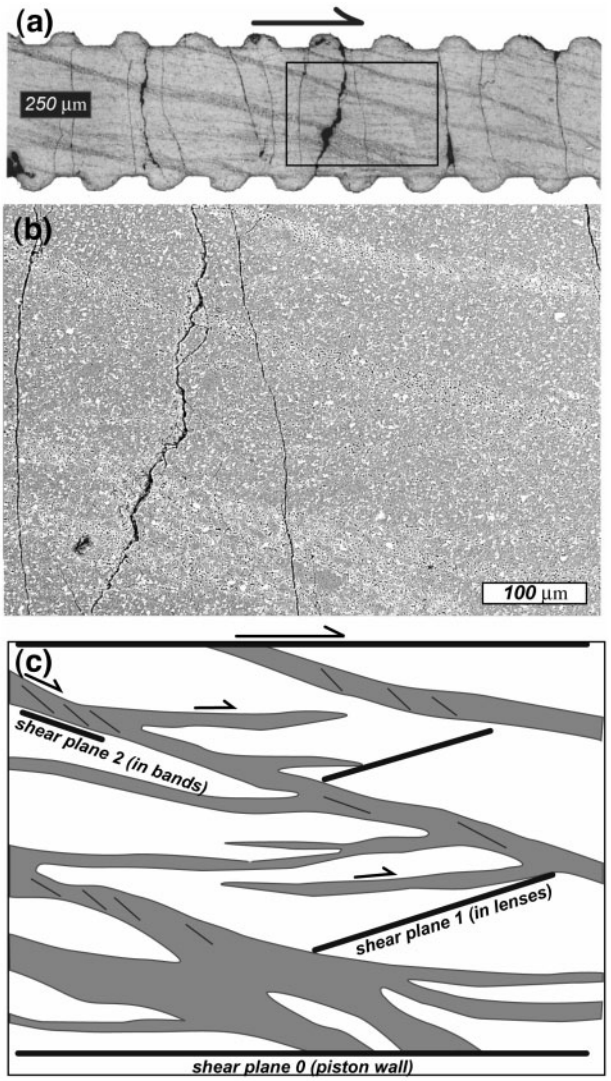

Fig. 13. Images of a sample (PI-l096) deformed at high constant strain rate, showing anastomosing network and multi-scale properties of melt distribution. (a) Reflected light image of the sample. The box marks the region magnified in (b). The melt-rich bands are dark grey linear regions oriented at 10–25° to the shear plane. (b) SEM-BSE image of the region outlined in (a). The white phase is chromite, the grey is olivine, and the black is MORB glass. The bands appear faintly as concentrations of black dots. (c) Schematic outlines of the band regions in (b). The dark lines show the approximate orientation of the shear planes in the sample as a result of strain partitioning and local reorientation of the stress field, as inferred from the orientation of secondary features, such as smaller bands and oriented melt pockets within the large bands, as illustrated in Fig. 5d.

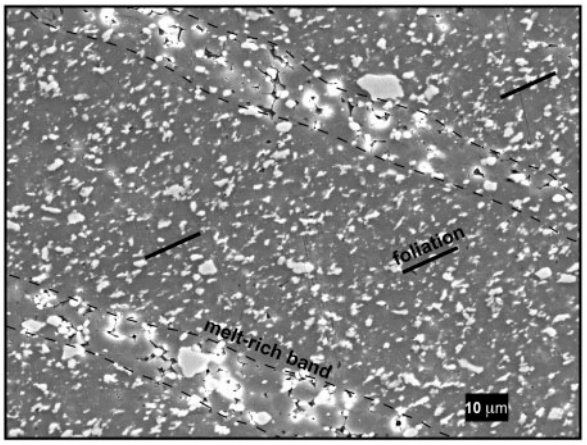

Fig. 14. SEM-BSE image of sample PI-l070, a sample with very low melt fraction ($\phi_t \sim 0{\cdot}005$). The scale bar represents 10 μm. The elongation of chromite particles in the lens regions with virtually no melt, with an elongation foliation as indicated, should be noted. In contrast, the chromites form euhedral grains in the melt-rich bands, implying that the melt allows an Ostwald ripening.

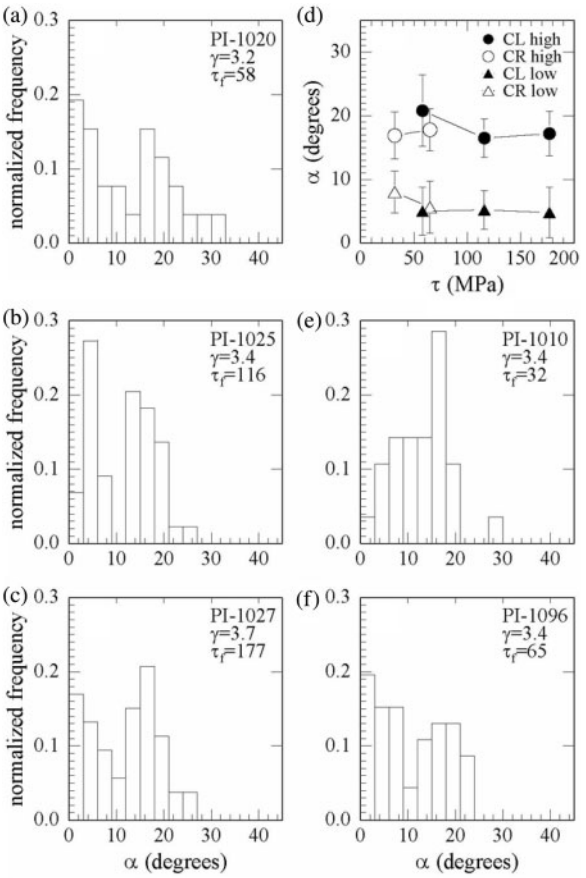

Fig. 15. Histograms of band angles for the CL and CR sets. (a–c) The CL set, with load increasing downward. (e and f) The CR set (PI-l096 is the sample deformed at higher strain rate). (d) The mean and standard deviation of the two populations of the bimodal distribution of band angles (high and low) for each sample are plotted as a function of stress.

rises with increasing strain. In the CR set, l096 is clearly in a steady state, because both strain rate and stress are approximately constant. PI-l020 (CL set, lowest stress) was quenched at approximately the same stress level as PI-l096 (CR set, faster strain rate). Interestingly, they have very similar band spacings, consistent with the idea that band spacing is set by stress, but very different values

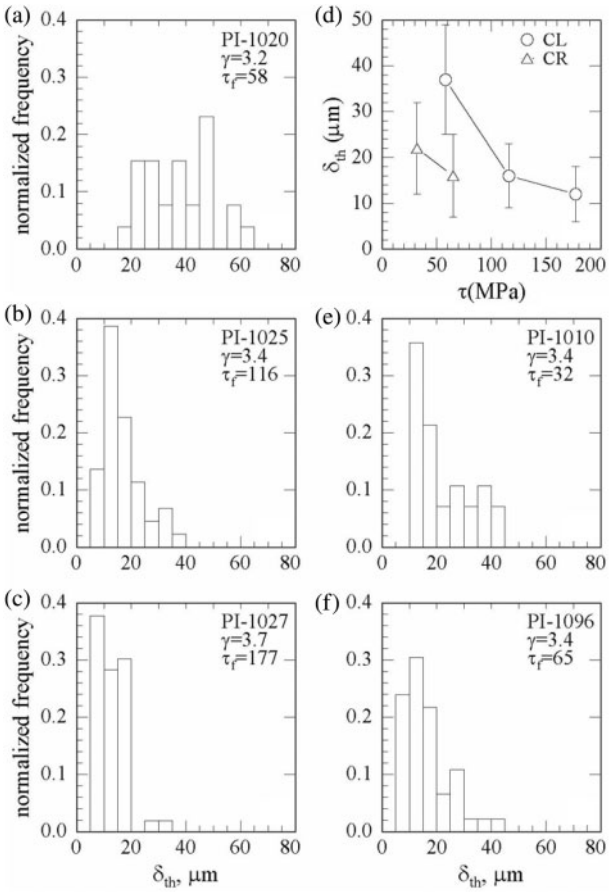

Fig. 16. Histograms of band thicknesses, δ_{th}, for the CL and CR sets. (a–c) The CL set, with load increasing downward. (e and f) The CR set, with strain rate increasing downward. (d) The mean and standard deviation of the distribution of band thicknesses for each sample plotted as a function of stress, τ.

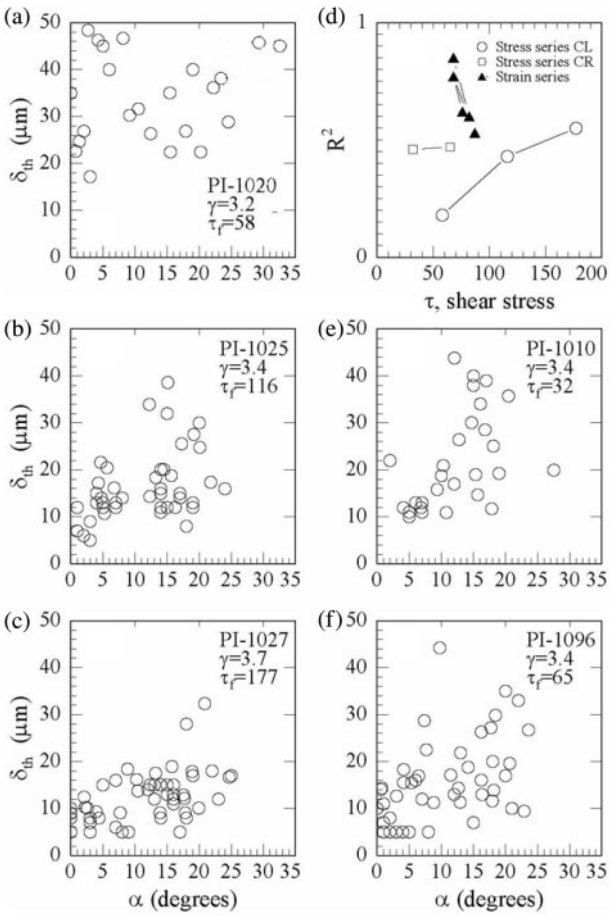

Fig. 17. Correlations of band angles and thicknesses for the CL and CR sets. (a–c) The CL set, with load increasing downward. (e and f) The CR set, with strain rate increasing downward. (d) Plot of correlation coefficient R^2 as a function of shear stress; in the stress series, the correlation is much weaker than that observed in the strain series.

for all other parameters, suggesting that PI-1020 is not in steady state. [Data from sample PI-1020 are often outliers, making interpretations ambiguous in such a small dataset. It is anomalous in its high values of a_b and ϕ_b (Table 7). It has an inordinately high melt fraction in the measured plane ($\phi_t^{local} = 0{\cdot}09$, much higher than $\phi_t^{global} = 0{\cdot}04$), which suggests that melt has flowed laterally into the plane of measurement. Therefore, the spacing may well be set by stress, but the other parameters, including δ_{th}, a_b, and ϕ_b may be changing with time and affected by lateral flow of melt in the sample.]

Summary

(1) The band angles have bimodal distributions. In the stress series, this bimodal pattern seems to be the key signature of a connected network (Fig. 15), whereas in the strain series, the signature was the correlation between α and δ_{th} (Fig. 8).

(2) Band thicknesses do not have normal distributions. They appear to have a power-law distribution, but the data are limited to less than one order of magnitude of length scale (Fig. 16). The mean of the thickness data in both CR and CL sets decreases with increasing stress.

(3) A correlation exists (although weaker) between band thickness and band angle. This correlation is much worse than that in the strain series, which may be an indication that in the thicker samples with no strain marker, the bimodality of the angles is configuration preferable to a strong correlation between angle and thickness (Fig. 17).

(4) The band spacings decrease with increasing stress, and data from CL and CR sets collapse onto one line as a function of stress, suggesting that band spacing is a direct function of stress. The band thicknesses seem

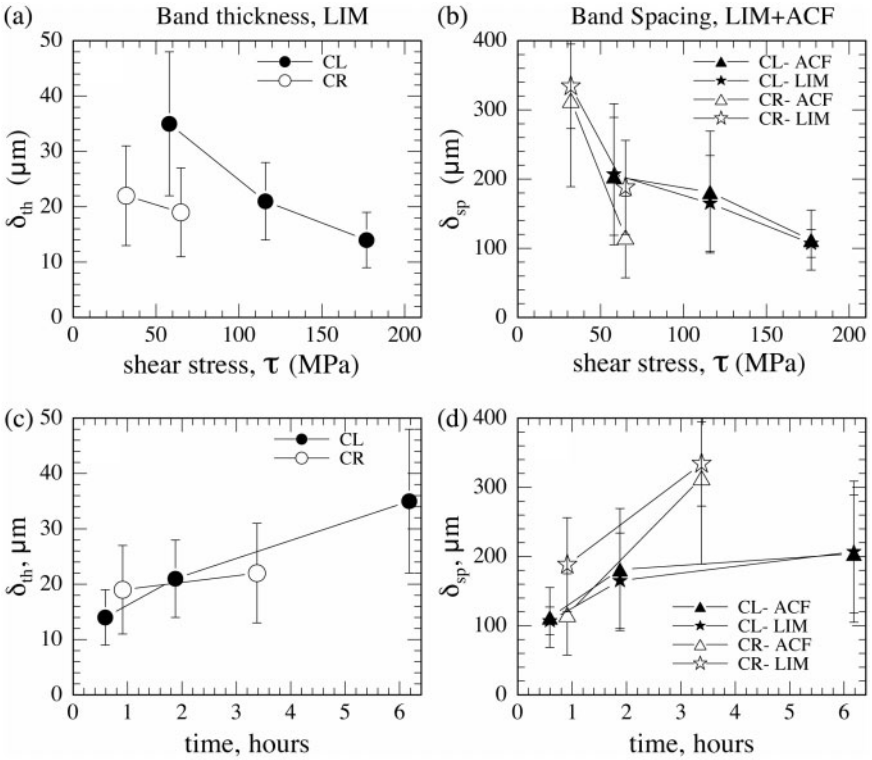

Fig. 18. Plots of band spacing, δ_{sp}, and thickness, δ_{th}, as functions of stress, τ, and experiment duration. (a) δ_{th} vs τ from the linear intercept method (LIM) measurements. (b) δ_{sp} vs τ data from the autocorrelation function (ACF) and LIM measurements. (c) δ_{th} vs time from LIM measurements. (d) δ_{sp} vs time from ACF and LIM measurements.

to vary more consistently as a function of the duration of the experiment (Fig. 18).

(5) Both a_b and ϕ_b increase with increasing duration of the experiment. The data from the constant load samples and constant rate samples collapse onto one line as a function of time, not stress. This pattern is consistent with δ_{th} changing with time, whereas δ_{sp} may be set by the value of stress (Fig. 19), suggesting that the melt distribution in each sample is not in steady state.

(6) In the CL set, stress always rises; in the CR set, stress can vary while strain rate is approximately constant. Only one sample, PI-1096 of the CR set, appears to be in a macroscopic steady state as indicated by constant stress and strain rate.

Summary of experimental results from both series

The data from the strain series clearly showed that (1) the melt is significantly segregated and networks begin to form by a shear strain of $\gamma \sim 1$, and (2) the networks are well formed by $\gamma \sim 2$. In the stress series, with the strain marker removed and the sample size increased, differences in network morphology between samples become more visible and meaningful. In the data on geometric and spatial properties of the melt distribution, there are distinct differences between the tightly constrained samples in the strain series and those in the stress series. In the strain series, the band angles (α) have normal distributions, the band thicknesses (δ_{th}) have log-normal or power-law distributions, and α and δ_{th} are tightly correlated. In contrast, in the stress series, the frequencies of bands at a given α have bimodal distributions, the distributions of δ_{th} appear to be more log-normal or power law, and α and δ_{th} are weakly correlated. Thus, in the strain series, the signature of the anastomosing network is the correlation of α and δ_{th} (Fig. 8), whereas in the stress series, the signature of the anastomosing network is the bimodal distribution of α (Fig. 17).

In the stress series, all the variations within and between the constant load set and the constant rate set can be attributed to differences in either applied stress or total duration of the experiment, because strain was kept approximately constant. Whereas the distributions of α are similar for all values of stress (τ) or experiment duration (t_f), there are significant differences in the other (average and geometric) properties of the melt distributions. We plotted the mean values of band spacing (δ_{sp}) and band thickness (δ_{th}), as well as the average properties of the melt configuration, a_b and ϕ_b, as functions of τ and t_f

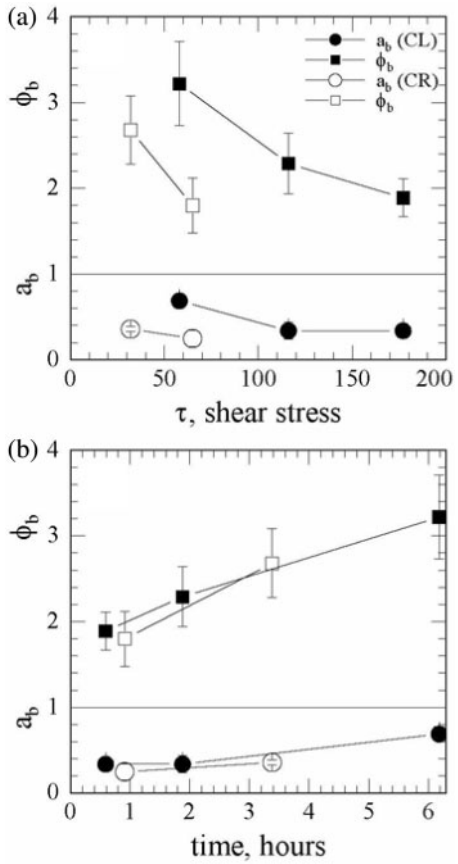

Fig. 19. (a) a_b and ϕ_b as a function of shear stress for the CL and CR series. (b) a_b and ϕ_b as a function of time for the CL and CR series.

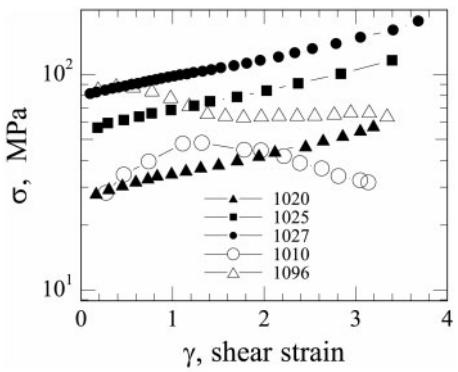

Fig. 20. Shear stress as a function of shear strain for the stress series experiments. CL set samples are filled symbols; CR set samples are open symbols.

for both sets. The data for δ_{sp} from both sets collapse to one line when plotted against stress, unlike the data for all the other parameters, which collapse onto one line as a function of t_f.

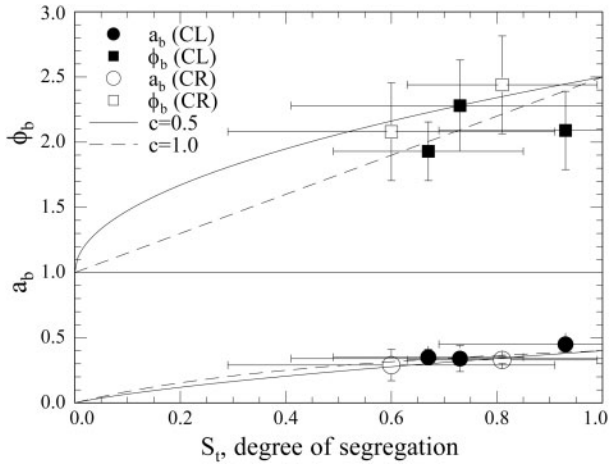

Fig. 21. Evolution of average melt distribution parameters a_b and ϕ_b with degree of segregation, S_t. The fits to these curves are from equations (11) and (12), with $a_{max} = 0{\cdot}4$ and $\phi_{max} = 2{\cdot}5$. These data have been adjusted to the local melt fraction, as discussed in the text, such that $S_t \leq 1$.

The results for S_t

The values of S_t and S_t^{local} are given in Table 7. In Fig. 21, we plot a_b and ϕ_b (both normalized values) as functions of S_t and overlay the functions from equations (11) and (12). With this limited dataset, we are not able to look for similarities and differences in these paths as functions of thermodynamic conditions (such as stress and melt fraction) and loading path (such as constant-load and constant-strain rate paths). However, the fits to these empirical expressions are good enough to allow us to use them in applications to thermodynamics of deformation (Holtzman *et al.*, 2005) and calculation of seismic properties (Holtzman & Kendall, in preparation).

DISCUSSION: OPEN QUESTIONS

In this study, we set out to address two broad questions: (1) How does the melt configuration evolve with increasing shear strain? (2) How does the applied stress level influence the melt configuration? We demonstrated that the bands form at shear strains of approximately $\gamma = 1$ and increasing stress level causes a decrease in the band spacing. The questions raised by the experiments fall into the following groups.

(1) Do the samples reach conditions of steady state deformation? All the following questions can be addressed most meaningfully if the data come from experiments that were quenched during steady state. The reason for this restraint is that thermodynamic driving forces are balanced.

(2) In the deforming system, what physical properties and/or driving forces control the observed melt distribution and degree of melt segregation? What

combination controls the scaling of melt distribution parameters measured in experiments?

(3) Mechanically speaking, how does melt organize? What are the deformation and transport processes controlling the dynamics of the self-assembly and organization?

(4) How do we scale to the conditions of the Earth? How can we extrapolate inference of processes from these observations to natural conditions?

Steady state?

In the study of this dynamic system, the identification of a steady state is a goal in the experiments. In terms of irreversible (non-equilibrium) thermodynamics, steady state requires that the rate of entropy production be minimized and the related quantity of viscous energy dissipation is time-invariant (i.e. $d\Phi/dt = 0$), (de Groot & Mazur, 1984, p. 43; Holtzman *et al.*, 2005), which means that stress, strain rate, and effective viscosity are time-invariant. Because effective viscosity is dependent on the melt distribution in a system with strain partitioning between bands and lenses, the distribution should also be statistically time-invariant. Thus, the clearest macroscopic indication of steady state is that stress and strain rate are both constant. As shown in Fig. 20, only one sample (PI-1096) achieves this state unambiguously.

Understanding the conditions required for steady state would reveal a great deal about the subprocesses that must be in balance in the system. To achieve true steady state, the rate of reorganization of melt must perfectly balance the rate of solid deformation, such that, on average, the distribution of band and lens sizes does not change; locally there is always redistribution of melt relative to solid, but across the sample, the statistical distributions of all these properties are constant. Below, we present a view of the events and processes that must be occurring to achieve a constant band angle, one quantity we know is constant in all experiments.

So then, if only one sample achieved a demonstrable steady state, how meaningful are the data? How far from steady state are the samples? Quantifying this question requires knowledge of the transient time scale for reorganization (relative to the inverse of the strain rate). We do not know yet, but we assume that the ratio is not too far from unity. The uncertainties in measurement and the crudeness of our current understanding of the scaling processes are within range of the variability in parameters caused by quenching the system at some distance from steady state. Thus, we proceed with a discussion of scaling by compaction length. We leave for future work the interpretation of experimental results in the framework of irreversible thermodynamics, as addressed by Holtzman *et al.* (2005).

Scaling by compaction length

With increasing stress, the band spacing δ_{sp} decreases. The length scales of many structural properties of materials (such as grain size, distance between dislocations, fracture spacings, etc.) have this relationship. There is not a self-consistent theoretical explanation for this scaling for all of these processes; each is described somewhat independently. For band spacing, compaction theory works fairly well. In an earlier study (Holtzman *et al.*, 2003*a*), we demonstrated that the spacing of the melt bands, δ_{sp}, scales with the compaction length, δ_c. One of the objectives of the stress series experiments was to provide a more controlled test of this scaling relationship.

δ_c is defined by the material transport properties internal to the system, simplified as two different viscosities and a permeability. As stated above, we want to understand how the stress controls the melt band spacing. If the processes are governed by two-phase flow, a compaction–decompaction process, then the compaction length should influence the observed distribution. The compaction length is defined as

$$\delta_c = \sqrt{k(\phi,d)\eta(\phi,d,\tau)/\mu} \qquad (13)$$

where k is the permeability, d is the grain size, η is the shear viscosity of the composite, μ is the shear viscosity of the melt, ϕ is the melt fraction and τ is the shear stress. In the stress series of experiments, we varied compaction length by changing the stress-dependent solid viscosity, using increasing values of load to push the system further into the dislocation creep regime, thus lowering the effective viscosity. In our earlier study (Holtzman *et al.*, 2003*a*), we calculated the initial compaction length, δ_c^o. In the present paper, all of the samples have the same initial melt fraction and grain size, and thus the same initial compaction length in the absence of stress. As soon as deformation begins and melt begins to segregate, the compaction length becomes stress-dependent and spatially variable. Thus, to compare the results from experiments with similar δ_c^o, we calculate the minimum compaction length at the end of the experiment, which occurs in the lenses where melt fraction is lowest. In our earlier study (Holtzman *et al.*, 2003*a*), we demonstrated that at high ϕ, the increase in k with increasing ϕ approximately offsets the decrease in η with increasing ϕ. In contrast, at low ϕ, the decrease in k with decreasing ϕ dominates, such that δ_c drops quickly. Because the minimum compaction length in the system should set the spacing, we estimate δ_c in the melt-depleted lenses. As discussed in Appendix B, we use the value of ϕ_n measured with the average properties; grain size d is measured in the strain series experiments (Table 4) to constrain the grain growth parameter, to account for grain growth during the experiment; k is calculated with the method discussed by Holtzman *et al.* (2003*a*); the composite viscosity is calculated using the flow law parameters reported by

Table 4: Experimental results for the 'strain' series

Sample	α	δ_{th} (LIM)	R^2	δ_{th} (ACF)	δ_{sp} (LIM)	δ_{sp} (ACF)
884	17 ± 6	24 ± 10	0·85	33 ± 19	—	57 ± 29
889	22 ± 13	30 ± 18	0·60	127 ± 84	—	163 ± 100
833	22 ± 6	27 ± 16	0·53	67 ± 15	97 ± 32	100 ± 19
885	—	—	—	42 ± 28	—	56 ± 29
891	17 ± 5	21 ± 9	0·77	89 ± 80	—	121 ± 101
830	17 ± 6	22 ± 12	0·62	162 ± 96	195 ± 32	183 ± 93

All lengths in microns; α in degrees.

Table 5: Experimental results for the 'stress' series

Sample	α	δ_{th} (LIM)	R^2	δ_{th} (ACF)	δ_{sp} (LIM)	δ_{sp} (ACF)
1020	13 ± 9	37 ± 12 (26)	0·18	117 ± 55	207 ± 102 (6)	204 ± 85
1025	11 ± 6	16 ± 7 (44)	0·43	108 ± 46	165 ± 69 (7)	181 ± 88
1027	11 ± 7	12 ± 6 (53)	0·55	67 ± 25	107 ± 20 (7)	112 ± 43
1010	12 ± 6	22 ± 10 (28)	0·46	90 ± 31	334 ± 61 (2)	313 ± 125
1096	10 ± 7	16 ± 9 (46)	0·47	57 ± 15	188 ± 68 (2)	116 ± 59

All lengths in microns. LIM refers to data obtained by the linear intercept method (see Appendix A). ACF refers to data obtained by calculating the autocorrelation function. Number of data points in parentheses.

Table 6: Average melt distribution characteristics for the 'strain' series

Sample	a_b	ϕ_b	S_t
884	$0{\cdot}50 \pm 0{\cdot}08$	$1{\cdot}6 \pm 0{\cdot}1$	$0{\cdot}80 \pm 0{\cdot}1$
889	$0{\cdot}39 \pm 0{\cdot}03$	$2{\cdot}3 \pm 0{\cdot}2$	$0{\cdot}90 \pm 0{\cdot}2$
833	$0{\cdot}42 \pm 0{\cdot}16$	$2{\cdot}3 \pm 0{\cdot}4$	$0{\cdot}97 \pm 0{\cdot}4$
885	$0{\cdot}44 \pm 0{\cdot}08$	$1{\cdot}5 \pm 0{\cdot}1$	$0{\cdot}66 \pm 0{\cdot}1$
891	$0{\cdot}27 \pm 0{\cdot}16$	$1{\cdot}5 \pm 0{\cdot}2$	$0{\cdot}41 \pm 0{\cdot}2$
830	$0{\cdot}44 \pm 0{\cdot}20$	$1{\cdot}6 \pm 0{\cdot}4$	$0{\cdot}70 \pm 0{\cdot}4$

Table 7: Average melt distribution characteristics for the 'stress' series

Sample	a_b	ϕ_b	ϕ_n	S_t	S_t^{local}	A_b^{local}	ϕ_b^{local}
1020	$0{\cdot}69 \pm 0{\cdot}08$	$3{\cdot}22 \pm 0{\cdot}49$	$0{\cdot}021 \pm 0{\cdot}005$	$2{\cdot}22 \pm 0{\cdot}36$	0·93	0·45	2·09
1025	$0{\cdot}34 \pm 0{\cdot}10$	$2{\cdot}29 \pm 0{\cdot}35$	$0{\cdot}014 \pm 0{\cdot}003$	$0{\cdot}81 \pm 0{\cdot}32$	0·77	0·34	2·28
1027	$0{\cdot}34 \pm 0{\cdot}06$	$1{\cdot}89 \pm 0{\cdot}22$	$0{\cdot}019 \pm 0{\cdot}003$	$0{\cdot}98 \pm 0{\cdot}18$	0·67	0·35	1·93
1010	$0{\cdot}36 \pm 0{\cdot}03$	$2{\cdot}68 \pm 0{\cdot}40$	$0{\cdot}015 \pm 0{\cdot}002$	$0{\cdot}98 \pm 0{\cdot}18$	0·80	0·33	2·44
1096	$0{\cdot}25 \pm 0{\cdot}10$	$1{\cdot}80 \pm 0{\cdot}32$	$0{\cdot}016 \pm 0{\cdot}003$	$0{\cdot}47 \pm 0{\cdot}24$	0·60	0·29	2·08

Hirth and Kohlstedt (2003) based on the values of stress at the end of the experiment (τ_f).

When compaction length is plotted in this manner, as shown in Fig. 23, we provide the following interpretation. Four data points plot tightly on a line with a slope of 2/5, similar to the scaling coefficient of 1/5 estimated by Holtzman *et al.* (2003*a*), if one data point (PI-1020) is considered an outlier. The difference in observed slope between the two studies (2/5 vs 1/5) may come from the difference in how δ_c is calculated; here, we calculate δ_c in the lenses at the end of the experiment (using τ_f and a flow law, and the measured melt fraction in the lenses, ϕ_n); in our earlier study (Holtzman *et al.*, 2003*a*), we calculated an initial δ_c (using a measured initial viscosity and the average ϕ_t). Thus, $\delta_c^o \neq \delta_c^{min}$. However, the basic idea that $\delta_{sp} < \delta_c$ remains.

The fact that compaction theory has successfully simulated basic aspects of this segregation and organization process (Katz *et al.*, 2006) lends further support to its use as a scaling parameter. The question now is why compaction theory works and what are its limitations. To address this question, we discuss our observations and intuitions into the processes active in these experimental systems.

Dynamics of melt segregation and organization

Here, we develop a conceptual model for melt migration and the evolution of the melt network organization. This model is a recipe for the maintenance of a steady state, and in that context, a framework for evaluating what processes must be in balance in a steady state. Simple shear (as opposed to pure shear), because of its highly rotational nature, poses complications that are not understood yet: What causes the stability of the distribution of band angles? Why does the segregation instability stabilize, such that all the melt is not drained from the lenses and small bands appear to be persistent? What causes the formation of an anastomosing network geometry and why? Earlier (Holtzman *et al.*, 2005), we introduced a model for a 'pumping mechanism' by which the melt network can maintain a constant distribution of band angles, and ultimately a steady state in all quantitative aspects. Here we expand on this model based on experimental observations. This mechanism has three elements, (1) nucleation; (2) rotation and growth and (3) closure, all of which are

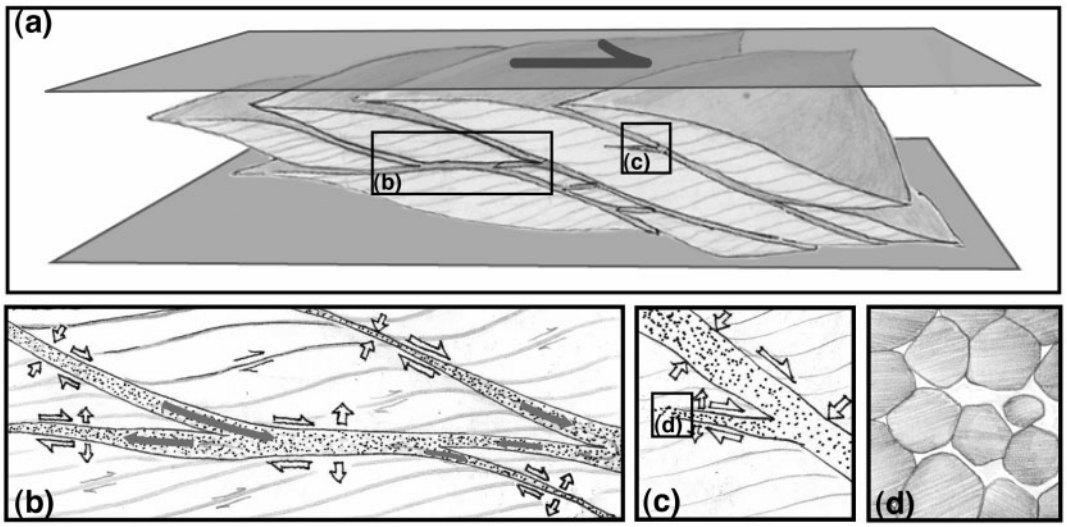

Fig. 22. The pumping mechanism. (a) A schematic illustration of lenses between two underformable plates. The light grey lines in the lenses are local shear planes and the melt-rich bands are transparent. (b) Inset in (a). The open arrows indicate stress orientations and the filled grey arrows indicate melt flow direction. We propose here and elsewhere (Holtzman *et al.*, 2005) that the normal stress components on the bands switch sign above some critical angle (>30°) from tensile or dilational to compressive or compactional, essentially because lenses have to deform more and more the closer a band is to 45°, and the system will only tolerate a certain stress difference between bands and lenses. This flattening of the bands causes the melt pressure to rise and sets up a flow into lower angle bands. (c) Inset in (a). Bands can nucleate and propagate into a lens at a low angle, and can also close off, as shown in Fig. 13. (d) Inset in (c). A grain-scale view of the tip of a propagating band.

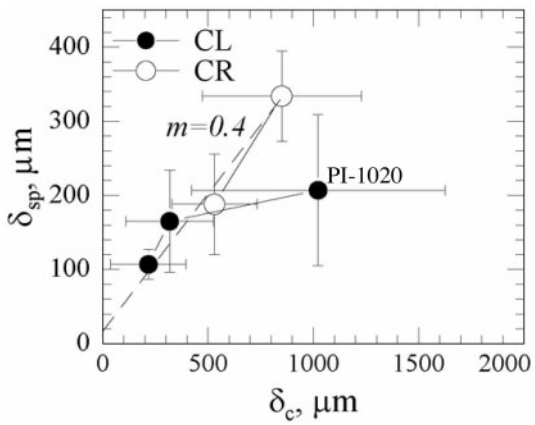

Fig. 23. Band spacing, δ_{sp}, as a function of compaction length, δ_c. PI-1020 appears to be an outlier, as discussed in the text. The slope of a linear fit to the rest of the data is $m = 0{\cdot}4$.

occurring simultaneously in a deforming sample, as illustrated in Fig. 22.

Nucleation

Why do bands nucleate and at what angle? Our observations from the lowest shear strain experiments in the strain series suggest that bands begin to form at 5–25°, with a mean and standard deviation of $18 \pm 6°$. In sheared samples of olivine + MORB, Zimmerman *et al.* (1999) found that melt pockets were elongated and oriented at approximately the same angle, suggesting that this angle is ubiquitous and is stress controlled (not controlled by the physical properties of the matrix). These observations suggest that bands form at the same distribution of angles at which they are observed when mature, by the collection and accumulation of individual elongated pockets. Hier-Majumder *et al.* (2004) adopted a micromechanical approach to this question, looking at how shear stress caused the growth of some pockets at the expense of others, and speculated that pockets at 0–45° to σ_1 open preferentially by stress corrosion, causing an average angle of ~ 20°. Nucleation of small bands within the well-developed lenses occurs at lower angle (5–10° relative to the shear plane), reflecting the local back-rotation of the stress field as a result of strain partitioning between lenses and bands. This local modification of stress fields was discussed extensively in an earlier study (Holtzman *et al.*, 2005). Once elongated pockets are nucleated, the stress-driven segregation instability is initiated.

Rotation and growth

As discussed by Holtzman *et al.* (2003*a*, 2005), Spiegelman (2003) and Katz *et al.* (2006), bands should rotate with shear if melt is not migrating relative to the solid. The apparent rotation is caused by the simple shear, but it is actually the shear parallel advection of a material line (melt-rich band) at an angle to the shear plane, causing the appearance of rotation. Spiegelman (2003) modified Stevenson's (1989) instability analysis from a pure shear to

a simple shear geometry and showed that if significant strain partitioning does not occur, bands should rotate as they grow up to 90° to the shear plane, with maximum growth rate at 45°. As bands rotate with shear upwards towards 45°, both the shear and normal stress diminish on them, causing mean pressure and thus melt pressure to drop, and thus causing more melt to flow in (Fig. 22b). As discussed by Holtzman *et al.* (2005), strain partitioning reduces this tendency to rotate and can stabilize bands at the observed angles. This partitioning does occur in the numerical models of Katz *et al.* (2006). Melt migration through the network reduces the need for band rotation; the more effective the melt transport in the network, the less rotation should occur.

Closure

The observation from both sets of experiments is that there are no bands at angles >30°. Therefore, the bands must close and the melt move elsewhere (into a lower angle band) before a band rotates up to 30°. We suggest that this closure is caused by increasing normal stress on the bands as they approach 45° as a result of strain partitioning, as discussed by Holtzman *et al.* (2005). The cause of this increase in normal stress is that as less deformation is accommodated in the bands, the deformation must increasingly be accommodated in the lenses, causing them to flatten, as illustrated in Figs 22b, c. As they flatten, the converging walls of the lenses increase the melt pressure in the bands, driving their compaction. In Fig. 14, the rounded chromite grains suggest that melt was previously present in that location and has since migrated away into a nearby band, as evidence for these closures. This migration from high- to low-angle bands also occurred in the models of Katz *et al.* (2006). This closure is the key to the pumping mechanism: the melt is driven into the low-angle bands. Therefore, they decompact and continue to rotate until they too are sufficiently compressed. The stress-driven 'instability' is thus stabilized.

Of course, this distinction between events is somewhat artificial, because all are happening together; in steady state, it is possible that the rotations are very small. However, the idea may help explain the observation that in the strain and stress series of experiments, the signature of the anastomosing network was different. In the strain series, it was the correlation of band angles and band thicknesses (Fig. 8). In the stress series, the signature was the bimodal distributions of band angles (Fig. 17). The relevant difference between the two series is probably in the relative freedom to organize. The more constrained boundary conditions in the strain series experiments may have forced more rotation and made migration more difficult. In the stress series, the greater degree of freedom of the bands allows them to organize more effectively into two populations, which allow the system to be closer to a steady state and a smaller need for rotation of melt bands (Fig. 13).

As melt is moving relative to the solid, all the matrix deformation processes required to accommodate local changes in melt fraction (i.e. deformation of the solid) must also be in balance. This balance is the principle of compaction theory (e.g. McKenzie, 1984). We have shown evidence that the mechanisms accommodating these deformations are different in the melt-depleted lenses and the melt-rich bands. In the lenses, the dominant deformation mechanisms are probably dislocation creep and dislocation-accommodated grain boundary sliding (GBS). Evidence for dislocation creep is the coexistence of a lattice preferred orientation (e.g. Holtzman *et al.*, 2003*b*) and for GBS are small generally euhedral grains, as well as the measured values of n from 1 to 3·5 (increasing with increasing applied stress). Further discussion of these mechanisms has been given by de Bresser *et al.* (2001), Goldsby & Kohlstedt (2001), Hirth & Kohlstedt (2003) and Warren & Hirth (2006). In the melt-rich bands, diffusion creep is probably enhanced by the large melt fractions relative to dislocation creep. As shown in Fig. 5, melt fraction can locally be very high, and the deformation mechanism may be one closer to a granular flow, in which grains slide past each other with little internal deformation but are always in contact. This kind of mechanism would probably be only local and transient, and speculatively, moving in waves along a band. As shown in Fig. 5, growth and dissolution features suggest that dissolution-precipitation (pressure solution) might also be a locally important deformation mechanism, especially in the bands. There is no evidence for brittle fracture or the opening of air-filled pore space. Any local dilatency (i.e. decompaction) is balanced by local melt flow and mass-balanced compaction.

Relation to other experimental studies

Numerous deformation experiments on partially molten rocks have been performed in uniaxial compression, but very few in (approximate) simple shear or in torsion. Of those studies on simple shear deformation of partially molten rocks (e.g. Dell'Angelo & Tullis, 1988; Zimmerman *et al.* 1999), rock analogues (e.g. Rosenberg & Handy, 2000), or rocks with water (e.g. Schmocker *et al.*, 2003; Hier-Majumder & Kohlstedt, 2006) conducted over a wide range of conditions within the ductile or semi-ductile regime, almost all display alignment of melt pockets controlled by the principal stress direction, but none to our knowledge have developed obvious melt-rich networks at length scales much longer than the grain size. In uniaxial compression experiments (e.g. Mecklenburgh & Rutter, 2003), melt pockets align but segregation at wavelengths longer than the grain scale does not occur either. Longer wavelength segregation may not occur because, in some cases, the compaction length is too small relative to the sample size (too close to the grain scale, $\delta_c \sim d$) as a result of the high melt viscosity (e.g. granitic systems) and in

others, because δ_c is larger than the sample size (e.g. possible samples with fluid water). However, segregation similar to that occurring here has been observed in partially molten metals (Gourlay & Dahle, 2007).

Experiments on analogue materials (i.e. camphor + melt) have potential for insight in the comparison of the behavior of two 'similar' materials at similar scaled conditions. In several studies, segregation occurs during pure (Takei, 2005) and simple shear (e.g. Rosenberg & Handy, 2000). In the former case, thin melt-rich layers form parallel to σ_1 and normal to σ_3. In the latter case, pockets align at 20° to the shear plane, and melt segregates and strain localizes into one layer (not a network) parallel to the shear plane; melt then flows out of this layer to the edges of the sample. The experiments were unconfined and drained, and the rheology was semi-brittle, so the physics governing the melt distribution is different from ours; thus a well-constrained comparison cannot yet be made.

We iterate here that there are similarities between the physical processes causing melt segregation and organization in our experiments and those in the materials deforming in more brittle or granular regimes. For example, in torsion experiments on aggregates of quartz plus water at 350 MPa and ~1300 K (Schmocker *et al.*, 2003), conditions at which quartz deforms in a semi-brittle fashion, water-rich bands formed that look macroscopically similar to ours. Microscopically, the mechanisms are different, as they are in a semi-brittle regime, so compaction length may not be a relevant quantity. The shear bands in these materials, classified as Riedel shears, generally exhibit an angle and morphology similar to ours. However, a Riedel shear is a classification of structure based on its orientation, but is not necessarily associated with a particular process or mechanism of formation. Thus, whether all fluid-rich bands at a particular angle occur for the same reason is not clear, but if this is so, it is likely to be related to the relationship between shear and normal stress on the band. For example, in dilating materials, the separation of grains and creation of air-filled space may reflect the same stress state as the separation of grains caused by increasing melt fraction. In other words, local dilatation balanced by nearby compaction in our samples may affect the stress state in the shear band in the same way that a global dilatancy does.

Applications to the Earth

Here we expand somewhat on the potential applications of these experimental results to the Earth (Holtzman *et al.*, 2003*a*, 2003*b*, 2005; Holtzman & Kendall, in preparation). First, can the stress-driven melt segregation process occur at the low melt fractions ($\phi \leq 0{\cdot}02$–$0{\cdot}03$) thought to occur in much of the partially molten region beneath a mid-ocean ridge (e.g. Kelemen *et al.*, 1997)? We have demonstrated in experiments that the process occurs at very low melt fractions ($\phi_t \leq 0{\cdot}005$), suggesting that it is very effective at segregating very small melt fractions. However, the stresses at which it occurs are higher than those that exist in the asthenosphere. Therefore, an important question is whether the process requires a yield stress to be surpassed? Below, we readdress our compaction length scaling arguments, with an analysis of the importance of surface tension, raising the question of whether the stress-driven segregation process occurs only after a yield stress has been reached. Then, we review relevant field observations that were not pointed out in our earlier study (Holtzman *et al.*, 2003). Finally we discuss a hypothetical application to ridge melting and melt transport in extensional settings, generalizable to other geodynamic settings.

Compaction length, surface tension, and yield stress

We have demonstrated here, with a series of better constrained experiments than used earlier (Holtzman *et al.*, 2003*a*), that the compaction length is a relevant scaling factor, which works well for scaling internally. However, scaling to the mantle is still a large leap (but not any more bold than scaling a laboratory-derived flow law). We have two immediate questions, as follows.

First, what is the influence of the sample size on the scaling? It is clear that the melt-rich networks are 'aware' of the boundaries of the system. Because the sample thickness is approximately constant in the experiments and the network spacings are not, δ_c is involved in determining δ_{sp}. Thus, taking this scaling one step further will require larger samples (e.g. in torsion geometry) and well-calibrated numerical models and analysis from which more sophisticated scaling rules can be derived (e.g. Katz *et al.*, 2006). For the moment, the compaction length is still the most reasonable scaling tool; the simple conclusion is that $\delta_{sp} < \delta_c$.

Second, for the segregation process to occur, does a yield stress have to be surpassed? If so, it is smaller than the lowest stress we achieved in these experiments (<25 MPa). If a yield stress does exist, what determines it? One possibility is that surface tension plays a role. If so, the yield stress should be much lower in the mantle than in the experiments, based on the following analysis.

Surface tension is significantly larger in the small grain sizes of these experiments than in the Earth. To estimate this effect, we revive the scaling of Cooper (1990). He estimated the pressure gradient driving melt migration as the result of competition between two driving forces, (1) shear stress gradient, the first term on the right-hand side of the following equation, and (2) surface tension (γ_{sl}), the second term on the right-hand side:

$$\frac{\partial p_s}{\partial y} = \left(\xi + \frac{4\eta}{3}\right)\frac{\partial \dot{\varepsilon}}{\partial y} - \frac{\partial(\gamma_{sl}/\phi^{1/2}d)}{\partial y}, \qquad (14)$$

where ξ is the bulk viscosity. In the following, the viscosity factor in parentheses is approximated as the melt-dependent composite shear viscosity.

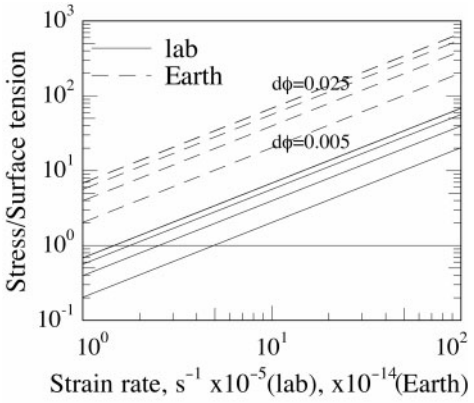

Fig. 24. Ratio of stress to surface tension forces (C^*) vs strain rates, grain sizes, and melt fraction differentials appropriate to the mantle and the laboratory. The group of continuous lines represents conditions for the laboratory strain rates, parameterized by $d\phi$, increasing from bottom up, as labelled for the set of dashed lines scaled to the Earth. Grain size is taken to be internally constant, but for the Earth, $d = 1000\,\mu$m and for laboratory conditions, $d = 10\,\mu$m. At low strain rates, in the laboratory, surface tension resists melt segregation; in the Earth, surface tension is minuscule.

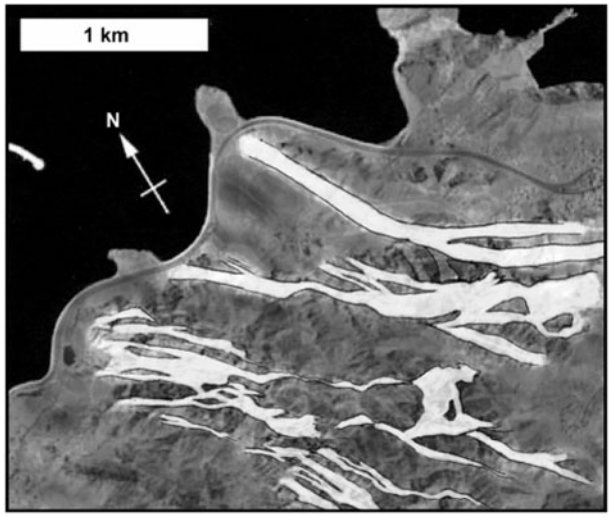

Fig. 25. An aerial IR photograph of part of the Oman ophiolite near Muscat, adapted from Braun & Kelemen (2002). Here we show only the trace of the dunites (light grey) surrounded by harzburgite (dark grey). The morphological similarities to our experiments (namely that smaller bands tend to join with larger bands at different angles) should be noted.

The ratio of the two driving forces, viscous stress over surface tension stress, is related to the Capillary Number (C) (e.g. Stone, 2004), so we call it C^*, where

$$C^* = \frac{\eta\left(\partial\dot{\varepsilon}/\partial y\right)}{\frac{\partial(\gamma_{sl}/\phi^{1/2}d)}{\partial y}} \approx \frac{\Delta\sigma}{\gamma_{sl}/\phi^{1/2}d}. \qquad (15)$$

We discretize the spatial gradients as

$$C^* = \frac{\dot{\varepsilon}\{\eta_0[\exp(-\alpha\phi_1) - \exp(-\alpha\phi_2)]\}}{\gamma_{sl}\left[1/d_1\phi_1^{1/2} - 1/d_2\phi_2^{1/2}\right]}. \qquad (16)$$

The ratio C^* in equation (16) is plotted vs strain rate in Fig. 24. We keep grain size constant (i.e. it is an additional parameter, but does not vary within a sample), but vary $d\phi$ spatially. The results indicate that in the laboratory, at low strain rates or stresses, stress dominates over surface tension; if the stress were removed, surface tension would be a significant driving force that would work against melt segregation. Thus, in the experiments, the stress-driven segregation requires non-negligible energy to work against surface tension (e.g. Parsons *et al.*, 2007). However, in the Earth, because of the much larger grain size, the surface tension force is much less significant, even relative to the much lower stresses. Thus, if surface tension causes a yield stress barrier for the process to occur in the Earth, the barrier is probably easily overcome in much of the asthenosphere. A value of $C^* > 1$ means that, as melt segregates significantly, stress gradients in the sample are still large enough to keep melt segregated. This relationship may affect the compaction length scaling coefficient, but probably not the validity of the idea.

Geological evidence for stress-driven melt segregation

The other approach to testing the applicability of the processes occurring in these experiments to the Earth is to look for evidence directly (e.g. Holtzman *et al.*, 2003*b*). In general, geological evidence for stress-driven melt segregation is abundant in exposures of formerly ductile, partially molten lower crust in oceanic and continental settings, although proving the existence of a dynamic process is difficult. Many structures in migmatites that show hypersolidus deformation may well be evidence of stress-driven melt segregation (e.g. Tommasi *et al.*, 1994; Neves *et al.*, 1996; Brown & Solar, 1998). Such preservation is more likely in the crust than in the asthenospheric and lithospheric mantle because, in the crust, melt viscosities are higher and temperature gradients are steeper. Evidence is more difficult to find in the mantle because melt extraction is generally more complete [for exceptions see Cannat *et al.* (1990) and references given by Holtzman *et al.* (2003*a*)]. Planar concentrations of plagioclase and/or clinopyroxene in dunite and harzburgite are suggestive of segregated, channelized melt (e.g. Boudier & Nicolas, 1995; Kelemen *et al*, 1997; Holtzman *et al.*, 2003*a*). A comprehensive review of length scales of melt segregation features in the lower crust and upper mantle, looking for correlations with stress estimates, is necessary for developing these ideas further.

Braun & Kelemen (2002) have shown that dunites deep in the mantle section in the Oman ophiolite form by melt migrating from below into shallow mantle rocks with

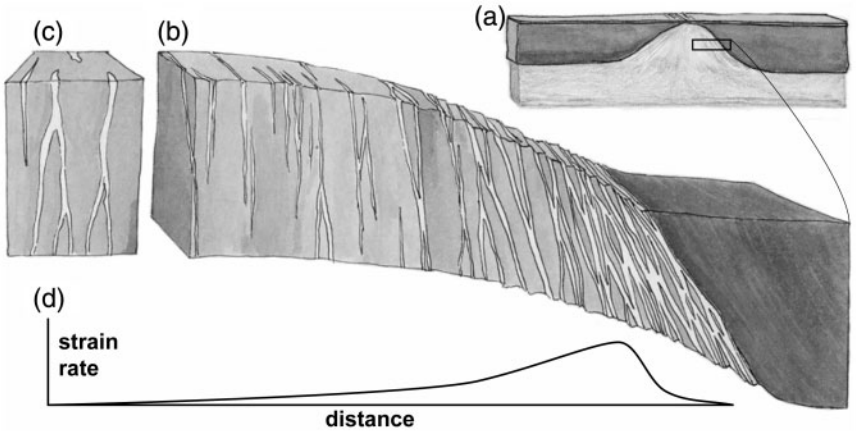

Fig. 26. A schematic illustration of a hypothetical spatial distribution of structures formed by stress-driven melt segregation beneath a mid-ocean ridge. (a) A plate-scale view of a mid-ocean ridge, with lithosphere darker than asthenosphere. (b) A gradient from lithosphere (right) to the middle of the melting region (left), crossing the abrupt transition from the compositionally (not thermally) defined lithosphere to a region of melt-rich bands. The degree of segregation increases from left to right, and so the effective composite viscosity should decrease. (c) In the center of the melting region (to the left), the strain rate should be a minimum, as shown in (d); the tubular form of these structures suggests that buoyancy is the dominant melt-driving force and the reaction–infiltration instability dominates stress-driven melt segregation (where strain rate is low enough). (d) Strain rate increases from the center of the melting region to the margins of the lithosphere. The implicit hypothesis is that S_t is increasing proportionally to strain rate, and viscosity is decreasing proportionally. The ideal configuration would allow deviatoric stress to be constant across the profile. In less than ideal configurations, stress gradients may exist that drive melt laterally, towards the walls. Seismic properties should also reflect these gradients.

which they are not in equilibrium. As the melt migrated to shallower depths, it dissolved clinopyroxene and precipitated olivine, causing a feedback between increasing dissolution and increasing melt flux (Kelemen *et al.*, 1995). However, modelling of the reaction infiltration instability that results in the formation of dunite channels predicts tubular, not planar, features (e.g. Aharonov *et al*, 1997). In Fig. 25, a tracing of a satellite photograph of a part of the Oman ophiolite with a large-scale melt-transport network illustrates that the smaller dunites have different orientations from the larger ones, and the smaller ones connect to the larger ones, both characteristics of the melt patterns observed in our experiments. We suggest that deviatoric stress and strain partitioning influenced melt distribution as the dunite-forming reaction progressed.

Geodynamics: an example application to mid-ocean ridges

The global mid-ocean ridge system is organized to transport heat from the Earth's interior to its exterior. Within the roughly triangular region of partially molten asthenosphere, from about 60–100 km below the oceanic crust up to the Moho, melt is formed and transported in increasing disequilibrium with its host rock as it rises and focuses towards the ridge axis (Fig. 26a). Most of the melt volume is not in equilibrium with the shallow upper mantle. Based on this observation and the rapid rates of melt ascent, melt must travel predominantly in high-flux channels, chemically separated from the surrounding rock. Here, we reiterate our proposition that the stress-driven segregation process may be very effective at segregating the deepest small melt fractions and becomes increasingly important in the parts of the ridge system closer to the flanks or boundaries of the system, where strain rates are higher because of corner flow and the rheological transition occurs from lithosphere to asthenosphere, as illustrated in Fig. 26b. A potentially testable prediction is that the transport will be most effective, and thus melt–rock disequilibrium greatest, at the flanks of the melt region, where deformation is most intense. This kind of approach can be adapted to any geodynamic environment, by making predictions about the locations of the greatest melt productivity and highest strain rates (Holtzman & Kendall, in preparation).

CONCLUSIONS

We have demonstrated that deviatoric stress drives melt to segregate into melt-rich networks. They develop after small strains and, as they form, progressively concentrate strain into them. Higher stress levels cause the characteristic spacings of the networks to decrease. We relate this decrease to a decrease in the minimum compaction length in the system. We propose a conceptual model for strain partitioning and melt pumping to maintain steady-state melt distributions. Scaling analyses applied to Earth conditions suggest that the process should be possible at the low stresses in the partially molten mantle and produce networks with spacings of the order of 10–1000 m. This process, if it occurs in the Earth, will strongly influence the

rheological, seismic, and melt transport properties of the upper mantle and lower crust.

ACKNOWLEDGEMENTS

We wish to thank Mark Zimmerman and members of the Kohlstedt laboratory for immeasurable help, Ben Greenhagen and Dan Moir for assistance with the melt distribution measurements, and Takehiko Hiraga and Florian Heidelbach for help with electron microscopy. Yasuko Takei generously and thoughtfully scrutinized this study. Valuable and critical reviews were provided by Julian Mecklenburgh, Michel Rabinowicz and Dan McKenzie. Funding for this research comes from NSF grants OCE-0327143 and OCE-0648020, and for B.K.H., a Fulbright Fellowship to France, UMN doctoral dissertation fellowship, and LDEO Postdoctoral Research Fellowship.

REFERENCES

Aharonov, E., Spiegelman, M. & Kelemen, P. (1997). Three-dimensional flow and reaction in porous media; implications for the Earth's mantle and sedimentary basins. *Journal of Geophysical Research, B, Solid Earth and Planets* **102**, 14821–14833.

Bercovici, D. & Ricard, Y. (2003). Energetics of a two-phase model of lithospheric damage, shear localization and plate-boundary formation. *Geophysical Journal International* **152**, 581–596.

Boudier, F. & Nicolas, A. (1995). Nature of the Moho Transition Zone in the Oman Ophiolite. *Journal of Petrology* **36**(3), 777–796.

Braun, M. & Kelemen, P. (2002). Dunite distribution in the Oman Ophiolite: implications for melt flux through porous dunite conduits. *Geochemistry, Geophysics, Geosystems* **3**(11), 8603, doi:10.1029/2001GC000289.

Brown, M. & Solar, G. (1998). Shear-zone systems and melts: feedback relations and self-organization in orogenic belts. *Journal of Structural Geology* **20**, 211–227.

Cannat, M., Bideau, D. & Hebert, R. (1990). Plastic-deformation and magmatic impregnation in serpentinized ultramafic rocks from the Garrett Transform-Fault (East Pacific Rise). *Earth and Planetary Science Letters* **101**, 216–232.

Chadam, J., Hoff, D., Merino, E., Ortoleva, P. & Sen, A. (1986). Reactive infiltration instability. *IMA Journal of Applied Mathematics* **36**, 207–221.

Connolly, J. A. D. & Podladchikov, Y. Y. (1998). Compaction-driven fluid flow in viscoelastic rock. *Geodinamica Acta* **11**, 55–84.

Cooper, R. (1990). Differential stress induced melt migration: an experimental approach. *Journal of Geophysical Research* **95**, 6979–6992.

Cooper, R. F. & Kohlstedt, D. L. (1984). Sintering of olivine and olivine–basalt aggregates. *Physics and Chemistry of Minerals* **11**, 5–16.

Daines, M. J. & Kohlstedt, D. L. (1994). The transition from porous to channelized flow due to melt–rock reaction during melt migration. *Geophysical Research Letters* **21**, 145–148.

Daines, M. J. & Kohlstedt, D. L. (1997). Influence of deformation on melt topology in peridotites. *Journal of Geophysical Research, B, Solid Earth and Planets* **102**, 10257–10271.

De Bresser, J. H. P., Ter Heege, J. H. & Spiers, C. J. (2001). Grain size reduction by dynamic recrystallization: can it result in major rheological weakening? *International Journal of Earth Sciences* **90**, 28–45.

de Groot, S. R. & Mazur, P. (1984). *Non-equilibrium Thermodynamics*. New York: Dover.

Dell'Angelo, L. N. & Tullis, J. (1988). Experimental deformation of partially melted granitic aggregates. *Journal of Metamorphic Geology* **6**, 495–515.

Fowler, A. C. (1990). A compaction model for melt transport in the Earth's asthenosphere. Part I: the basic model. In: Ryan, M. P. (ed.) *Magma Transport and Storage*. New York: John Wiley, pp. 4–14.

Goldsby, D. L. & Kohlstedt, D. L. (2001). Superplastic deformation of ice: Experimental observations. *Journal of Geophysical Research—Solid Earth* **106**, 11017–11030.

Gourlay, C. M. & Dahle, A. K. (2007). Dilatent shear bands in solidifying metals. *Nature* **445**, doi:10.1038/nature05426.

Hall, C. E. & Parmentier, E. M. (2000). Spontaneous melt localization in a deforming solid with viscosity variations due to water weakening. *Geophysical Research Letters* **27**, 9–12.

Hier-Majumder, S. & Kohlstedt, D. L. (2006). Role of dynamic grain boundary wetting in fluid circulation beneath volcanic arcs. *Geophysical Research Letters* **33**, doi:10.1029/2006GL025716.

Hier-Majumder, S., Leo, P. H. & Kohlstedt, D. L. (2004). On grain boundary wetting during deformation. *Acta Materialia* **52**(12), 3425–3433.

Hirth, G. & Kohlstedt, D. L. (1995a). Experimental constraints on the dynamics of the partially molten upper mantle 2. Deformation in the dislocation creep regime. *Journal of Geophysical Research* **100**, 15441–15449.

Hirth, G. & Kohlstedt, D. L. (1995b). Experimental constraints on the dynamics of the partially molten upper mantle: Deformation in the diffusion creep regime. *Journal of Geophysical Research* **100**, 1981–2001.

Hirth, G. & Kohlstedt, D. (2003). Rheology of the upper mantle and the mantle wedge: a view from the experimentalists. In: Eiler, J. (ed.) *Inside the Subduction Factory. American Geophysical Union, Geophysical Monograph* **138**, 324 p.

Holtzman, B. K., Groebner, N. J., Zimmerman, M. E., Ginsberg, S. B. & Kohlstedt, D. L. (2003a). Stress-driven melt segregation in partially molten rocks. *Geochemistry, Geophysics, Geosystems* **4**, 8607.

Holtzman, B. K., Kohlstedt, D. L., Zimmerman, M. E., Heidelbach, F., Hiraga, T. & Hustoft, J. (2003b). Melt segregation and strain partitioning: implications for seismic anisotropy and mantle flow. *Science* **301**, 1227–1230.

Holtzman, B., Phipps Morgan, J. & Kohlstedt, D. L. (2005). Viscous energy dissipation and strain partitioning in partially molten rocks. *Journal of Petrology* **46**(12), 2569–2592, doi:10.1093/petrology/egi065.

Hustoft, J. W. & Kohlstedt, D. L. (2006). Metal–silicate segregation in deforming dunitic rocks. **7**(2), doi:10.1029/2005GC001048.

Katz, R. F., Spiegelman, M. & Holtzman, B. (2006). The dynamics of melt and shear localization in partially molten aggregates. *Nature* **442**, doi:10.1038/nature05039.

Kelemen, P. B. & Dick, H. J. B. (1995). Focused melt flow and localized deformation in the upper mantle; juxtaposition of replacive dunite and ductile shear zones in the Josephine Peridotite, SW Oregon. *Journal of Geophysical Research, B, Solid Earth and Planets* **100**, 423–438.

Kelemen, P. B., Shimizu, N. & Salters, V. J. M. (1995). Extraction of mid-ocean-ridge basalt from the upwelling mantle by focused flow of melt in dunite channels. *Nature* **375**, 747–753.

Kelemen, P. B., Hirth, G., Shimizu, N., Spiegelman, M. & Dick, H. J. B. (1997). A review of melt migration processes in the adiabatically upwelling mantle beneath oceanic spreading ridges. *Philosophical Transactions of the Royal Society of London, Series A* **355**, 283–318.

Kohlstedt, D. L. & Zimmerman, M. E. (1996). Rheology of partially molten mantle rocks. *Annual Review of Earth and Planetary Sciences* **24**, 41–62.

McKenzie, D. (1984). The generation and compaction of partially molten rock. *Journal of Petrology* **25**, 713–765.

Mecklenburgh, J. & Rutter, E. H. (2003). On the rheology of partially molten synthetic granite. *Journal of Structural Geology* **25**, 1575–1585.

Mei, S., Bai, W., Hiraga, T. & Kohlstedt, D. L. (2002). Influence of melt on the creep behavior of olivine–basalt aggregates under hydrous conditions. *Earth and Planetary Science Letters* **201**, 491–507.

Neves, S. P., Vauchez, A. & Archanjo, C. J. (1996). Shear zone-controlled magma emplacement or magma-assisted nucleation of shear zones? Insights from noertheast Brazil. *Tectonophysics* **262**, 349–364.

Nicolas, A. (1986). A melt extraction model based on structural studies in mantle peridotites. *Journal of Petrology* **27**, 999–1022.

Parsons, R., Hustoft, J., Holtzman, B., Zimmerman, M. & Kohlstedt, D. L. (2007). An experimental and numerical study of surface tension-driven melt flow. *Earth and Planetary Science Letters* (in press).

Paterson, M. S. (1990). Rock deformation experimentation. In: Duba, A. G., Durham, W. B., Handin, J. W. & Wang, H. F. (eds) *The Brittle–Ductile Transition in Rocks; the Heard Volume. American Geophysical Union, Geophysical Monograph* **56,** 187–194.

Phipps Morgan, J. & Holtzman, B. K. (2005). Vug waves: a mechanism for coupled rock deformation and fluid migration. *Geochemistry, Geophysics, Geosystems* **6**(8), doi:10.1029/2004GC000818.

Press, W. H., Teukolsky, S. A., Vetterling, W. T. & Flannery, B. P. (1992). *Numerical Recipes in Fortran 77.* Cambridge: Cambridge University Press.

Rabinowicz, M. & Vigneresse, J.-L. (2004). Melt segregation under compaction and shear channelling: Application to granitic magma segregation in a continental crust. *Journal of Geophysical Research* **109**, doi:10.1029/2002JB002372.

Renner, J., Viskupic, K., Hirth, G. & Evans, B. (2003). Melt extraction from partially molten peridotites. *Geochemistry, Geophysics, Geosystems* **4**(5), 8606, doi:10.1029/2002GC000369.

Richardson, C. N. (1998). Melt flow in a variable viscosity matrix. *Geophysical Research Letters* **25**, 1099–1102.

Rosenberg, C. L. & Handy, M. R. (2000). Synthectonic melt pathways during simple shearing of a partially molten rock analogue (norcamphor–benzamide). *Journal of Geophysical Research B* **105**, 3135–3149.

Rubin, A. M. (1998). Dike ascent in partially molten rock. *Journal of Geophysical Research* **103**, 20901–20919.

Rutter, E. H. & Neumann, D. H. K. (1995). Experimental deformation of partially molten Westerly granite under fluid-absent conditions, with implications for the extraction of granitic magmas. *Journal of Geophysical Research* **100**, 15697–15715.

Schmocker, M., Bystricky, M., Kunze, K. & Burlini, L. (2003). Granular flow and Riedel band formation in water-rich quartz aggregates experimentally deformed in torsion. *Journal of Geophysical Research* **108**, 2242.

Scott, D. R. & Stevenson, D. J. (1984). Magma solitons. *Geophysical Research Letters* **11**, 1161–1164.

Spiegelman, M. (2003). Linear analysis of melt band formation by simple shear. *Geochemistry,. Geophysics, Geosystems* **4**(9), doi:10.1029/2002GC000499.

Spiegelman, M. & Kenyon, P. (1992). The requirements for chemical disequilibrium during magma migration. *Earth and Planetary Science Letters* **109**, 611–620.

Stevenson, D. J. (1989). Spontaneous small-scale melt segregation in partial melts undergoing deformation. *Geophysical Research Letters* **16**, 1067–1070.

Stone, H. A. (2004). Dynamics of drop deformation and breakup in viscous fluids. *Annual Review of Fluid Mechanics* **26**, 65–102, doi:10.1146/annurev.fl.26.010194.000433.

Takei, Y. (2005). Deformation-induced grain boundary wetting and its effects on the acoustic and rheological properties of partially molten rock analogue. *Journal of Geophysical Research* **110**, B12203, doi:10.1029/2005JB003801.

Tommasi, A., Vauchez, A., Fernandes, L. A. D. & Porcher, C. C. (1994). Magma-assisted strain localization in an orogen-parallel transcurrent shear zone of southern Brazil. *Tectonics* **13**, 421–437.

Vigneresse, J. L. (1999). Strain partitioning during partial melting and crystallizing felsic magmas. *Tectonophysics* **312**, 117–132.

Warren, J. M. & Hirth, G. (2006). Grain size sensitive deformation mechanisms in naturally deformed peridotites. *Earth and Planetary Science Letters* **248**, 423–435.

Zimmerman, M. E. & Kohlstedt, D. L. (2004). Rheological properties of partially molten lherzolite. *Journal of Petrology* **45**, 275–298.

Zimmerman, M. E., Zhang, S., Kohlstedt, D. L. & Karato, S.-i. (1999). Melt distribution in mantle rocks deformed in shear. *Geophysical Research Letters* **26**, 1505–1508.

APPENDIX A: MEASURING THE MELT DISTRIBUTION

Linear intercept method

With low-resolution photomicrographs, such as Figs. 2, 4, 10 and 11, we measured band angle (α) and band thickness (δ_{th}) with a 'linear intercept method' (LIM). As illustrated in Fig. 9a, lines are drawn across the sample at an orientation that is approximately normal to the bands, spaced far enough apart to minimize repeated measurements on one band. (Qualitatively, we consider the properties of a band to change on one side of a large junction with another band.) Wherever the line crosses a band, we draw a right angle composed of a line tangent to the band and one that traverses the thickness of the band and measure the angle and thickness.

In samples with a Ni strain marker, the melt bands form in regions between the nearest corner of a piston and the edge of the impermeable Ni strain marker. We analyzed the statistics of the melt distributions in these regions, cutting off the length equivalent to one sample thickness from each of the ends, to minimize measuring statistics of organization associated with these end-effects. In samples without a strain marker, we measured in the center of the samples.

Autocorrelation function and band spacing

To quantify the band spacings, δ_{sp}, in a way that is less subjective than the linear intercept method (as a check), we extract linear profiles normal to the band lengths

from the smoothed melt distribution images. The autocorrelation function is a method for extracting amplitude content at different frequencies by comparing a signal with itself

$$A(x) = \langle f(r)f(r+x) \rangle \tag{17}$$

(Press *et al.*, 1992, p. 492), where f is the signal, x is the spatial variable and r is the lag. The function f is multiplied by itself and divided by the total number of points (the meaning of the angular brackets). Then the signal is shifted by r and the summation and averaging is repeated for all values of r, from zero to N, where N is the total number of points in f. The result is a vector of length N, plotted as a function of the lag, r, as shown in Fig. 2e.

APPENDIX B: CALCULATING STRESS-DEPENDENT COMPACTION LENGTH

There are many parameters that go into the compaction length calculation. The main difference between what we have done here and in our earlier study (Holtzman *et al.*, 2003*a*) is to use the final compaction length in the lenses, calculated from measured melt fraction in the lenses and the final applied stress. The melt fraction enters into the permeability and the composite shear viscosity; the stress enters into the viscosity calculation.

Permeability

The permeability is calculated as discussed in the Appendix of Holtzman *et al.* (2003*a*). We use an anisotropic permeability model based on the observations of strongly aligned melt pockets in our samples and in those of Daines & Kohlstedt (1997) and Zimmerman *et al.* (1999), as discussed by Holtzman *et al.* (2003*a*);

$$k_{ij} = \begin{bmatrix} k_{11} & 0 \\ 0 & k_{33} \end{bmatrix} \tag{18}$$

where k_{11} is normal to the shear plane, and each component can be described by the equation $k = \phi^a d^m / b$ where $m = 2$ and values for a and b depend on direction. For k_{11}, $a = 3$ and $b = 25$, approximated as sheets. For k_{33}, $a = 2$ and $b = 10\,000$, approximated as tubes. Because k_{33}, the minimum, should be oriented roughly normal to the bands, we use this component as a scalar value in permeability in the compaction length.

Viscosity

The strain rate of a melt-free rock at experimental conditions may be described by a flow law of the form (Zimmerman & Kohlstedt, 2004)

$$\dot{\gamma}_{\phi=0} = A\tau^n d^{-p} \exp\left(\frac{-Q}{RT}\right) \tag{19}$$

where A is the pre-exponential term, τ is the shear stress (the final value in any dataset), d is the grain size, R is the gas constant and T is absolute temperature. Grain sizes were measured in two samples using a linear intercept method, before and after deformation (PI-830: $d_o = 9 \pm 3$ μm, $d_f = 12 \pm 5$ μm; PI-833: $d_o = 8 \pm 3$ μm, $d_f = 12 \pm 6$ μm). We use the final value for all samples. In fact, the composite dislocation and diffusion creep flow law is required to fit the data:

$$\dot{\gamma}_T = \dot{\gamma}_{\text{disl}} + \dot{\gamma}_{\text{diff}} \tag{20}$$

and the non-linear weakening effect of melt on the viscosity, often parameterized with the expression

$$\dot{\gamma}(\phi) = \dot{\gamma}_{\phi=0} \exp(\lambda\phi) \tag{21}$$

an equation based on an empirical fit to experimental creep data (Zimmerman & Kohlstedt, 2004). Finally, using the parameters listed in the following table,

$$\eta_t = \left(\frac{1}{\eta_{\text{diff}}} + \frac{1}{\eta_{\text{disl}}}\right)^{-1} \tag{22}$$

from Hirth and Kohlstedt (2003).

Table AI

	A	n	p	Q	λ
Dislocation—GBS	4·7e10*	3·5	2	600e3	32
Diffusion	1·5e9	1	3	375e3	30

*Units = $\mu m^p / (MPa^n\ s)$.